The Astronomical Journal, 170:266 (16pp), 2025 November https://doi.org/10.3847/1538-3881/ae0586

Survey of S-type AGB Stars Using the KVN Four-band Receiving System: SMASTES II

Seong-Min Son[1,2], Se-Hyung Cho[2,3], Jaeheon Kim[3], Hyeon Baek[1,3], Dong-Hwan Yoon[3], and Kyung-Won Suh[1]
[1] Department of Astronomy and Space Science, Chungbuk National University, Cheongju-City, 28644, Republic of Korea
[2] Department of Physics and Astronomy, Seoul National University, Gwanakgu, Seoul 08826, Republic of Korea; cho@kasi.re.kr
[3] Korea Astronomy and Space Science Institute, 776 Daedeok–daero, Yuseong–gu, Daejeon 34055, Republic of Korea
Received 2025 August 7; revised 2025 September 8; accepted 2025 September 8; published 2025 October 13

Abstract

We present the observational results of Simultaneous Multi-mAser Survey Toward Evolved Stars (SMASTES) II for 150 S-type asymptotic giant branch stars. Observations have been performed from 2023 September to 2024 March using the upgraded wide four-band (22/43/86/129 GHz) receiving system of the Korean VLBI Network. For simultaneous observations, 19 molecular lines of H_2O and multitransitions of SiO masers including several thermal lines were set up together. H_2O maser was not detected from any stars among 150 S-type stars. For SiO $v = 1$: $J = 1$–0, $J = 2$–1, and $J = 3$–2 masers were detected from nine, thirteen, and six stars, respectively. For SiO $v = 2$: $J = 1$–0, $J = 2$–1, and $J = 3$–2 masers were detected from five, two, and two stars, respectively. In particular, for $v = 1$: $J = 1$–0, $J = 2$–1, and $J = 3$–2 masers were all detected from five stars. For SiO $v = 0$: $J = 1$–0, $J = 2$–1, and $J = 3$–2 lines in ground vibrational state were detected from five, six, and seven stars, respectively, including the ^{29}SiO $v = 0$: $J = 1$–0 and $J = 2$–1 lines. For SiO $v = 0$: $J = 1$–0, $J = 2$–1, and $J = 3$–2 lines were detected in more stars at higher rotational transition lines. The carbon-bearing molecule HCN was detected from four stars. Based on these observational results, we perform statistical analyses on detection rates of maser and thermal lines, maser properties, and kinematics comparing with the results of M-type stars (SMASTES I). The characteristics of maser properties are investigated in the IRAS two-color diagram in relation to the evolutionary stage.

Unified Astronomy Thesaurus concepts: Asymptotic giant branch stars (2100); Late stellar evolution (911); Astrophysical masers (103); Interstellar thermal emission (857)

Materials only available in the online version of record: machine-readable table

1. Introduction

Asymptotic giant branch (AGB) stars are divided into two distinct groups on the basis of the photospheric carbon-to-oxygen ratio (C/O), O-rich (M-type, C/O $<$ 1), and C-rich (C-type, C/O $>$ 1) stars. Since normal stars and the interstellar medium have C/O $<$ 1, AGB stars start by having an atmosphere that is abundant in oxygen. However, as the AGB stars evolve, the thermal pulse spurred on by the He-shell flash and the subsequent third dredge-up events alter the chemical composition of the surface, causing them to become C-rich stars (C/O $>$ 1.0). Therefore, they pass through the transition phase, S-type stars (C/O $\sim$ 1.0), between O-rich M-type stars and C-rich stars. S-type stars are identified by the absorption bands of ZrO and LaO molecules with C/O ratios close to unity (I. Iben & A. Renzini 1983), indicating characteristics of s-process element enrichments (P. C. Keenan 1954; V. V. Smith & D. L. Lambert 1990). The s-process enrichments in S-type stars can be explained by the third dredge-up during the thermally pulsing AGB (TP-AGB) phase (T. B. Ake 1979; P. R. Wood et al. 1983; K.-W. Suh 2021). S-type stars can be further classified into "intrinsic" S-type stars, which are genuine TP-AGB objects showing technetium (Tc) lines, and "extrinsic" S-type stars, which are Tc-poor binaries thought to have acquired their overabundances via mass transfer from a former AGB companion (A. Jorissen & G. R. Knapp 1998; S. Van Eck et al. 2000, 2017).

As an S-type star evolves, it can undergo spectral type changes sequentially M-MS-S-SC-C, showing the gradual increase in both carbon abundances and s-process elements (B. Plez et al. 2003). The transition from O-rich to C-rich stars has a significant impact on the chemistry of circumstellar material associated with SiO and H_2O maser properties, including the properties of dust grains. S-type stars are interesting for investigating the onset and distribution of circumstellar masers, since small changes in molecular composition around C/O $\approx$ 1 can dramatically alter excitation processes (B. Gustafsson et al. 2008; G. Raskin et al. 2011; Y.-S. Ting et al. 2018). However, S-type stars have been studied only rarely through observations. Particularly, there were very few observational studies of H_2O and SiO masers compared to O-rich M-type stars.

Detection results collected from the literature for SiO, H_2O, and OH maser emission in S-type stars were presented by A. Jorissen & G. R. Knapp (1998). Nine S-type stars with SiO maser detections were listed, while no H_2O maser was detected in S-type stars. In the case of OH masers, 1612 MHz maser detection from RS Cnc was reported by G. M. Rudnitskij (1976), but it was not confirmed in other OH maser lines. Observational results of the SiO ($v = 1$, $J = 2$–1) toward 24 S-type stars were given by S. Ramstedt et al. (2009), listing 13 S-type stars with SiO maser detections, including four new detections. For the SiO $v = 2$, $J = 2$–1 maser, known to be an anomalously weak maser, V. Bujarrabal et al. (1996) reported 10 detected S-type stars, including eight new detections, based on observations of 15 S-type stars with the IRAM 30 m telescope. They confirmed a clear trend favoring the SiO $v = 2$, $J = 2$–1 maser in S-type stars compared to O-rich M-type stars, explained as the effects of IR line overlap between rovibrational SiO and H_2O lines proposed by H. Olofsson et al. (1981). For VLBI observations, the first

Table 1
List of Observed Sources

No.	Source Name	R.A. (J2000) (h:m:s)	Decl. (J2000) (d:m:s)	sp Type	$V_\star$ (km s^{-1})	T_A^* (peak) SiO	T_A^* (peak) CO	C/O	References
(1)	(2)	(3)	(4)	(5)	(6)	(7)	(8)	(9)	(10)
1	W Cet	00 02 07.390	−14 40 33.03	S5.5-7/1.5-3e	13	⋯	⋯	⋯	(2)
2	IW Cas	00 02 44.222	+48 42 50.81	S4-5.5/6e	−19	⋯	⋯	⋯	(1)
3	X And	00 16 09.593	+47 00 44.48	S2.5-5/6-7e	−4	⋯	⋯	⋯	(1)
4	BB And	00 17 43.953	+45 08 52.08	S3e	0	⋯	⋯	⋯	(1)
5	T Cet	00 21 46.273	−20 03 28.89	M5-6Se	22	⋯	7.90 (2–1)	⋯	(4, 6, 10)
6	R And	00 24 01.946	+38 34 37.37	S5-7/4-5e	−16.5	10.5[a]	⋯	⋯	(3, 6, 8)
7	U Cas	00 46 21.373	+48 14 39.87	S4.5-6/3-5e	−40	⋯	⋯	⋯	(9)
8	V661 Cas	00 46 54.586	+63 56 05.92	S	−65.55	⋯	⋯	⋯	(1)
9	RW And	00 47 18.920	+32 41 08.25	S6/2e	−15	⋯	⋯	⋯	(1)
10	OS Cas	00 50 38.462	+60 13 07.26	S	−58.77	⋯	⋯	⋯	(1)
11	RR And	00 51 23.281	+34 22 36.29	S6-7/3-3.5e	−71	⋯	⋯	⋯	(1)
12	V340 Cas	00 54 29.228	+48 21 26.24	S	−60.26	⋯	⋯	⋯	(1)
13	V365 Cas	01 00 53.153	+56 36 45.16	S6/3	−2.1	⋯	⋯	⋯	(2)
14	CR Psc	01 05 12.211	+19 11 52.04	M2wkS	−5.55	⋯	⋯	⋯	(1)
15	V418 Cas	01 12 59.799	+62 10 46.93	S7/2e	0	⋯	⋯	⋯	(1)
16	S Cas	01 19 41.980	+72 36 40.85	S3-54-8	−31	8.5[a], 2.3[b]	37.60	⋯	(3, 6, 8)
17	RX Psc	01 25 39.177	+21 23 46.04	S	−28.41	⋯	⋯	⋯	(7)
18	RZ Per	01 29 42.166	+50 51 23.89	S3-7/7-8e	−10	⋯	⋯	⋯	(1)
19	V401 Per	02 02 15.827	+52 33 40.88	S6/1	−7.48	⋯	⋯	⋯	(1)
20	CX Per	02 14 47.933	+51 48 18.22	S3wkS	0	⋯	⋯	⋯	(1)
21	W And	02 17 32.961	+44 18 17.76	S7-8/1e-M7Se	−35	31.0[a], 0.4[b]	8.14	⋯	(3, 6)
22	SU Tri	02 18 10.330	+31 44 57.09	S4.5/1+	67.99	⋯	⋯	⋯	(1)
23	DI Per	02 22 36.326	+54 09 21.50	MS	0	⋯	⋯	⋯	(1)
24	BI And	02 25 54.341	+38 07 22.14	S8/4.5v	−22.07	⋯	⋯	⋯	(1)
25	V835 Cas	03 07 15.068	+65 28 04.55	Sr	−6.86	⋯	⋯	⋯	(1)
26	V667 Cas	03 20 56.078	+70 46 38.76	S!	0	⋯	⋯	⋯	(1)
27	LZ Per	03 33 41.594	+48 59 41.59	S	4.77	⋯	⋯	⋯	(11)
28	WX Cam	03 49 03.742	+53 10 59.13	S5/5.5	−2.57	⋯	⋯	⋯	(1)
29	FG Per	03 53 30.220	+47 39 03.17	S	−29	⋯	⋯	⋯	(1)
30	HX Per	04 13 01.139	+45 26 13.35	S	−32.81	⋯	⋯	⋯	(1)
31	V1139 Tau	04 15 24.124	+24 04 42.52	S	3.27	⋯	⋯	⋯	(5)
32	NX Per	04 23 39.352	+49 57 26.10	S	0	⋯	⋯	⋯	(1)
33	GS Per	04 23 59.627	+41 56 27.72	Sp	0	⋯	⋯	⋯	(1)
34	WY Cam	04 39 53.462	+79 07 50.49	S2e	−28.54	⋯	⋯	⋯	(1)
35	T Cam	04 40 08.869	+66 08 48.64	S5-6/5e	−12.2	1.3[a]	1.06	⋯	(3, 4)
36	TV Aur	04 58 08.213	+48 33 37.07	S5/6	21.596399	⋯	⋯	⋯	(9)
37	GP Ori	05 02 48.066	+15 19 12.66	SC7/8	86	⋯	⋯	⋯	(5)
38	EI Tau	05 46 56.518	+17 54 30.99	S	0	⋯	⋯	⋯	(1)
39	BB Tau	05 52 18.607	+25 49 41.66	SC7/7e	2.17	⋯	⋯	⋯	(1)
40	V1623 Ori	05 52 27.864	+06 20 53.06	S	59.07	⋯	⋯	⋯	(11)
41	BB Aur	06 03 25.041	+31 38 40.88	M3S	−52.58	⋯	⋯	⋯	(1)
42	KR Cam	06 04 01.998	+59 32 18.95	S!	−46.4	⋯	⋯	0.96	(7)
43	GH Aur	06 09 27.713	+28 29 43.50	Swk	0	⋯	⋯	0.84	(7)
44	V376 Aur	06 12 01.719	+46 06 40.08	Swk	28.13	⋯	⋯	0.84	(7)
45	FU Mon	06 22 23.852	+03 25 27.89	S6.5/7.5	−41.7	⋯	9.8 (2–1)	⋯	(2, 5, 10)
46	CF Gem	06 27 15.340	+18 04 23.61	S	42.75	⋯	⋯	0.98	(7)
47	NP Aur	06 28 01.802	+36 04 59.04	M5	0	⋯	⋯	⋯	(7)
48	OY CMa	06 28 55.898	−11 50 60.00	S-2e-MS	0	⋯	⋯	⋯	(1)
49	V355 Cma	06 32 52.308	−26 10 23.87	S	0	⋯	⋯	⋯	(7)
50	CO Gem	06 33 55.569	+21 32 04.30	S	20.97	⋯	⋯	⋯	(1)
51	DY Gem	06 35 57.811	+14 12 46.03	S8,5	−16	⋯	4.70 (2–1)	⋯	(2, 6, 10)
52	CX Mon	06 37 18.479	+00 55 16.29	S6:/5+	16.5	⋯	⋯	⋯	(1)
53	V372 Mon	06 41 26.131	−04 35 45.78	SC7/7.5	14.5	⋯	⋯	⋯	(1)
54	GR Aur	06 43 42.602	+38 01 53.56	M5S	0	⋯	⋯	⋯	(1)
55	EN Mon	06 55 40.123	−05 31 02.64	S	57.7	⋯	⋯	⋯	(1)
56	BZ Cma	06 56 45.400	−25 53 42.11	S	80.97	⋯	⋯	0.99	(7)
57	GT CMa	06 59 44.739	−16 10 17.31	S-3	0	⋯	⋯	⋯	(1)
58	R Gem	07 07 21.271	+22 42 12.75	S3.5-6.5/6e	−59.1	⋯	⋯	⋯	(2, 6)
59	R Cmi	07 08 42.612	+10 01 26.46	SC4-7/10e	46.1	⋯	⋯	⋯	(9)
60	WX CMi	07 11 57.551	+07 29 58.80	M6Se	0	⋯	⋯	⋯	(1)
61	AA Cam	07 14 52.070	+68 48 15.36	M5S	−43.5	⋯	⋯	⋯	(2)

Table 1
(Continued)

No.	Source Name	R.A. (J2000) (h:m:s)	Decl. (J2000) (d:m:s)	sp Type	$V_\star$ (km s^{-1})	T_A^* (peak) SiO	T_A^* (peak) CO	C/O	References
(1)	(2)	(3)	(4)	(5)	(6)	(7)	(8)	(9)	(10)
62	XY Cmi	07 16 43.287	+03 06 58.37	S-3	0	⋯	⋯	0.71	(7)
63	RR Mon	07 17 31.542	+01 05 41.55	S8,2-M6Se	23	⋯	⋯	⋯	(2)
64	DT CMa	07 17 40.994	−14 12 59.41	S	27.65	⋯	⋯	⋯	(1)
65	V786 Mon	07 19 25.922	−00 43 28.41	S	0	⋯	⋯	⋯	(1)
66	V685 Mon	07 20 47.624	−07 48 09.61	S	36.46	⋯	⋯	⋯	(1)
67	BX CMa	07 25 05.871	−20 33 45.28	S	47.29	⋯	⋯	⋯	(1)
68	KN Mon	07 25 50.841	−10 41 07.82	S	45.12	⋯	⋯	⋯	(1)
69	FX CMa	07 27 03.936	−11 43 14.44	S5/6	0.19	⋯	⋯	⋯	(1)
70	Y Lyn	07 28 11.617	+45 59 26.23	M6S	−0.5	⋯	⋯	⋯	(6)
71	KP Mon	07 30 06.803	−10 53 20.91	S	78.86	⋯	⋯	⋯	(1)
72	GG Pup	07 38 21.107	−16 03 18.85	S5/5	29.96	⋯	⋯	⋯	(1)
73	T Gem	07 49 18.174	+23 44 04.09	S2-6/3-4e	22	⋯	⋯	⋯	(11)
74	NQ Pup	07 53 05.270	−11 37 29.35	S4.5/2	−2.12	⋯	⋯	⋯	(5)
75	AO Gem	07 56 56.010	+31 10 02.28	S!e	−6	⋯	⋯	0.96	(7)
76	EW Pup	07 59 16.041	−23 58 52.74	Se	0	⋯	⋯	⋯	(1)
77	EX Pup	08 00 38.313	−20 59 35.29	S24e	0	⋯	⋯	0.71	(7)
78	V Cnc	08 21 42.823	+17 17 06.47	S0-6/6e	−4.6	⋯	⋯	⋯	(11)
79	FT Pup	08 25 42.702	−23 37 13.98	S-2	0	⋯	⋯	⋯	(1)
80	SZ Pyx	08 33 08.404	−17 58 54.98	S	69.65	⋯	⋯	⋯	(1)
81	CO Pyx	08 45 08.964	−25 59 08.43	S43	0	⋯	⋯	⋯	(7)
82	CP Pyx	08 52 42.827	−25 14 44.34	S-5	0	⋯	⋯	⋯	(1)
83	RS Cnc	09 10 38.797	+30 57 47.29	M6S	7.7	⋯	6.72	⋯	(5)
84	FM Hya	09 43 31.378	−18 34 28.80	M0S	0	⋯	⋯	⋯	(5)
85	EY Leo	10 50 30.754	+10 19 48.86	M3S	−20.76	⋯	⋯	⋯	(1)
86	S Uma	12 43 56.676	+61 05 35.50	S0.5-6/6e	18	⋯	⋯	⋯	(5)
87	AV CVn	13 21 18.736	+43 59 13.70	S3/4	−77.62	⋯	⋯	⋯	(1)
88	R Cam	14 17 51.036	+83 49 53.84	S2-6.5/2.5-6e	−33	⋯	⋯	⋯	(1)
89	ST Her	15 50 46.623	+48 28 58.85	M6S-M7SIII:	−4.4	⋯	⋯	⋯	(2)
90	ST Sco	16 36 36.219	−31 14 02.43	S8/4.5	−4	⋯	10.8	⋯	(2, 4, 6, 10)
91	S Her	16 51 53.919	+14 56 30.76	M4-7.5Se	−10	⋯	⋯	⋯	(9)
92	FT Ser	17 21 40.985	−14 36 20.71	S5,8	−19.78	⋯	⋯	⋯	(1)
93	V812 Oph	17 41 31.939	+06 43 41.33	S5+/2.5	9.99	⋯	⋯	⋯	(11)
94	OP Her	17 56 48.527	+45 21 03.06	M6S	10.55	⋯	⋯	⋯	(9)
95	V679 Oph	18 41 57.169	+06 49 07.20	S5/5+	−45.77	⋯	⋯	⋯	(9)
96	V427 Sct	18 42 59.862	−04 28 19.84	S	0	⋯	⋯	⋯	(1)
97	TU Dra	18 51 30.132	+48 54 42.97	M6S	−42	⋯	⋯	⋯	(7)
98	SV Sct	18 53 40.968	−14 11 38.34	SC3	15.16	⋯	⋯	⋯	(1)
99	VX Aql	19 00 09.608	−01 34 56.72	SC5/8e	6.7	⋯	⋯	⋯	(2)
100	ST Sgr	19 01 29.197	−12 45 34.10	S6-7.5/2.5e	55.7	4.8[a], 2.8[b]	8.0 (2–1)	⋯	(2, 3, 6, 10)
101	S Lyr	19 13 11.805	+26 00 27.85	SC	49	⋯	⋯	⋯	(2, 4, 6, 8)
102	W Aql	19 15 23.357	−07 02 50.33	S6/6e	−26	20.4[a], 9.8[b]	44.92	⋯	(2, 3, 6, 8, 10)
103	V354 Aql	19 15 56.924	+00 37 32.24	M7S	−2.44	⋯	⋯	⋯	(1)
104	T Sgr	19 16 14.436	−16 58 17.08	S4.5-6/5.5-6e	9	⋯	2.4 (2–1)	⋯	(2, 4, 6, 10)
105	V734 Cyg	19 24 46.710	+44 28 56.48	M2-6Se	0	⋯	⋯	⋯	(7)
106	TT Sgr	19 25 34.094	−20 06 54.79	M8wkS	13	⋯	⋯	⋯	(1)
107	V1318 Aql	19 26 28.604	+08 47 10.83	S	0	⋯	⋯	⋯	(1)
108	EP Vul	19 33 17.837	+23 39 19.51	S6.5/5	0	⋯	⋯	⋯	(2, 6, 8)
109	SU Aql	19 36 00.303	+04 05 24.93	S	39.41	⋯	⋯	⋯	(1)
110	R Cyg	19 36 49.358	+50 11 59.73	S4-8/6e	−18.5	1.8[a]	15.6	⋯	(3, 6)
111	V4421 Sgr	19 42 47.804	−20 11 45.01	S34	0	⋯	⋯	⋯	(1)
112	XY Cyg	19 48 37.182	+41 37 52.09	Se	−2.72	⋯	⋯	⋯	(1)
113	V1717 Aql	19 49 01.506	+00 29 11.57	S!r	0	⋯	⋯	⋯	(7)
114	χ Cyg	19 50 33.921	+32 54 50.58	S6-9/1-2e	1.6	253.0[a], 141.9[b]	32.2	⋯	(2, 3, 6, 8)
115	V1766 Cyg	19 51 21.533	+43 34 57.56	M3-5III	0	⋯	⋯	⋯	(1)
116	V1407 Aql	19 57 16.879	−11 14 16.55	M6S	0	⋯	⋯	⋯	(1)
117	CM Cyg	19 58 34.253	+52 05 45.79	S4/6.5e	0	⋯	⋯	0.99	(7)
118	V899 Aql	20 01 29.447	+04 25 36.42	S	0	⋯	⋯	⋯	(7)
119	AA Cyg	20 04 27.606	+36 49 00.46	S6/3	11.4	⋯	⋯	⋯	(2, 6)
120	S Cyg	20 05 29.981	+57 59 08.67	S6/3.5e	−17	⋯	⋯	⋯	(1)
121	DK Vul	20 06 33.952	+24 26 00.13	S4,2	0	⋯	⋯	⋯	(2, 6)
122	SZ Cep	20 09 57.557	+77 11 09.58	S4-6/6e	−51.63	⋯	⋯	⋯	(1)

Table 1
(Continued)

No.	Source Name	R.A. (J2000) (h:m:s)	Decl. (J2000) (d:m:s)	sp Type	$V_\star$ (km s^{-1})	T_A^* (peak) SiO	T_A^* (peak) CO	C/O	References
(1)	(2)	(3)	(4)	(5)	(6)	(7)	(8)	(9)	(10)
123	V335 Sge	20 14 20.561	+17 00 54.74	S6/1	−23.78	⋯	⋯	⋯	(1)
124	V1190 Cyg	20 16 20.411	+54 09 15.31	MS	−34.26	⋯	⋯	⋯	(1)
125	V2012 Cyg	20 17 11.055	+31 33 18.08	S3,1	−18.74	⋯	⋯	⋯	(1)
126	V865 Aql	20 23 54.641	+00 56 44.79	S7,2	0	⋯	⋯	⋯	(1)
127	V441 Cyg	20 27 08.115	+36 33 06.50	S4,6	0	⋯	⋯	⋯	(1)
128	AD Cyg	20 31 36.513	+32 33 52.36	S5/5	2.6	⋯	⋯	⋯	(6)
129	Z Del	20 32 39.004	+17 27 04.11	S4.5/2e	34	⋯	⋯	⋯	(9)
130	FF Cyg	20 38 51.706	+37 53 23.23	S5.5/6-e	13.43	⋯	⋯	⋯	(1)
131	CY Cyg	20 46 50.245	+46 03 06.93	SC2 Zr0	2.69	⋯	⋯	⋯	(2)
132	V1976 Cyg	20 47 43.379	+34 19 03.27	S	−2.68	⋯	⋯	⋯	(1)
133	BV Vul	20 57 12.441	+29 20 03.84	S6.5/6-	−1.13	⋯	⋯	⋯	(1)
134	V1542 Cyg	20 59 23.234	+47 44 42.60	S	0	⋯	⋯	⋯	(1)
135	V471 Cyg	21 07 07.757	+38 34 05.31	S5.5/5.5	−3.22	⋯	⋯	⋯	(1)
136	V575 Cyg	21 09 19.266	+46 10 27.37	S	−57.86	⋯	⋯	⋯	(1)
137	V365 Cep	21 30 42.452	+61 33 26.44	S!	−20.4	⋯	⋯	⋯	(1)
138	V1338 Cyg	21 35 04.601	+40 51 25.28	Sr	0	⋯	⋯	⋯	(1)
139	V633 Cyg	21 36 26.893	+47 23 01.36	S	−34.64	⋯	⋯	⋯	(1)
140	CE Lac	22 43 44.878	+43 26 00.30	Swk	0	⋯	⋯	0.70	(7)
141	GY Lac	22 47 46.171	+55 18 13.02	S	0	⋯	⋯	⋯	(7)
142	V358 Lac	22 47 46.341	+43 43 58.62	S	0	⋯	⋯	⋯	(11)
143	CV Cep	22 49 54.441	+59 39 35.27	S5-7/1.5-2	−40.4	⋯	⋯	⋯	(11)
144	RX Lac	22 49 56.899	+41 03 04.31	S7.5/1e	−22.35	⋯	⋯	⋯	(2, 4, 6)
145	PR And	23 15 23.460	+50 18 54.41	S!	−8.68	⋯	⋯	⋯	(1)
146	BG And	23 30 59.424	+43 15 54.84	S5-7/3e	−33.42	⋯	⋯	⋯	(1)
147	V441 Cas	23 39 58.771	+63 20 54.50	S	−56.32	⋯	⋯	⋯	(1)
148	PT Cep	23 40 22.393	+70 26 29.61	M6S	0	⋯	⋯	⋯	(1)
149	EO Cas	23 51 27.293	+62 51 47.13	Se	−51	5.1[a]	⋯	⋯	(3)
150	WY Cas	23 58 01.306	+56 29 13.48	S6-6.5/6-e	2	14.5[a]	1.47	⋯	(2, 3, 4)

Notes. (1) C. B. Stephenson (1984); (2) R. Sahai & S. Liechti (1995); (3) V. Bujarrabal et al. (1996); (4) M. A. T. Groenewegen & T. de Jong (1998); (5) A. Jorissen & G. R. Knapp (1998); (6) S. Ramstedt et al. (2009); (7) K. Smolders et al. (2012); (8) T. Danilovich et al. (2018); (9) P. S. Chen et al. (2019); (10) M. Andriantsaralaza et al. (2021); (11) J. Chen et al. (2022). A conversion factor of 4.8 Jy K^{-1} at 155 GHz was applied for RS Cnc to convert antenna temperature (T_A^*) to flux density. $\boldsymbol{V}_*$: stellar velocity.
[a] SiO $v = 2$, $J = 2$–1.
[b] SiO $v = 1$, $J = 2$–1.

(This table is available in machine-readable form in the online article.)

VLBA images of SiO ($v = 1, 2$, $J = 1$–0 and $J = 2$–1) masers were reported for χ Cyg (R. Soria-Ruiz et al. 2004), showing that the SiO $v = 1$, $J = 2$–1 maser region was comparable to that of the $v = 1$, $J = 1$–0 maser, whereas the location of the SiO $v = 1$, $J = 2$–1 maser in the O-rich OH/IR star WX Psc was further out. They suggested this difference is due to the effects of IR line overlap (H. Olofsson et al. 1981). W. D. Cotton et al. (2010) performed VLBA observations of the SiO $v = 1, 2$, $J = 1$–0 masers at seven stellar phases of χ Cyg, showing comparable SiO ring diameters for $v = 1, 2$, $J = 1$–0 masers, varying from about 30 mas to 43 mas depending on stellar phases.

For thermal-line observations toward S-type stars, R. Sahai & S. Liechti (1995) performed CO $J = 1$–0 and/or $J = 2$–1 observations for 47 S-type stars, detecting CO lines in 29 stars. The mean expansion velocity was slightly lower compared to C-rich stars. S. Ramstedt et al. (2009) presented mass-loss rates and circumstellar SiO abundances for 40 S-type stars, reporting similar mass-loss distributions to M-type and C-rich stars, and that circumstellar SiO abundance is independent of the C/O ratio for a given mass-loss rate and expansion velocity. Using the ACA, M. Andriantsaralaza et al. (2021) measured CO ($J = 2$–1 and 3–2) circumstellar envelope sizes of 16 S-type stars and investigated deviations from spherical symmetry. For HCN, F. L. Schöier et al. (2013) presented multitransition survey results from M-type, S-type, and carbon stars, including 19 S-type stars, showing that HCN abundance correlates with C/O ratio.

About O-rich M-type stars, through the Simultaneous Multi–mAser Survey Toward Evolved Stars (SMASTES) I project, simultaneous 22/43/86/129 GHz observations were performed using the upgraded Korean VLBI Network (KVN) single-dish wideband receiving system toward 155 objects as a standard for comparative maser analysis (H. Baek et al. 2025). As the SMASTES II project, we have performed simultaneous 22/43/86/129 GHz observations of 150 S-type stars with KVN. The recent KVN wideband system offers many advantages for simultaneous observations of H_2O and various SiO masers along with thermal lines.

Through SMASTES II, we will statistically investigate the following: the detectability rate for 22 GHz H_2O maser and the reason for its nondetection in S-type stars, unlike M-type stars

Table 2
SMASTES-II Frequency Setting

Stream Num	Test Freq. (MHz)	Transition	Bandwidth (MHz)	rms Noise (Jy)	T_{sys} (K)	Velocity Resolution (km s^{-1})	Channel
(1)	(2)	(3)	(4)	(5)	(6)	(7)	(8)
1	22235.0798	H_2O $6_{1,6}$–$5_{2,3}$	64	0.07 ∼ 0.77	⋯	⋯	4096
2	22482.5480	SO_2 $v = 0$, $J_{Ka,Kc} = 24_{4,20}$–$23_{5,19}$	64	0.07 ∼ 0.75	61 ∼ 238	0.21	4096
3	42373.4266	^{30}SiO $v = 0$, $J = 1$–0	64	0.08 ∼ 0.81	⋯	⋯	4096
4	42519.3400	SiO $v = 3$, $J = 1$–0	64	0.07 ∼ 0.71	⋯	⋯	4096
5	42820.4800	SiO $v = 2$, $J = 1$–0	64	0.06 ∼ 0.79	⋯	⋯	4096
6	42879.8200	^{29}SiO $v = 0$, $J = 1$–0	64	0.06 ∼ 0.81	⋯	⋯	4096
7	43122.0300	SiO $v = 1$, $J = 1$–0	64	0.07 ∼ 0.76	75 ∼ 277	0.11	4096
8	43423.7600	SiO $v = 0$, $J = 1$–0	64	0.08 ∼ 0.74	⋯	⋯	4096
9	48990.9549	CS $v = 0$, $J = 1$–0	64	0.06 ∼ 0.83	⋯	⋯	8192
10	85640.4600	SiO $v = 2$, $J = 2$–1	64	0.08 ∼ 0.78	⋯	⋯	8192
11	85759.1990	^{29}SiO $v = 0$, $J = 2$–1	64	0.07 ∼ 0.85	⋯	⋯	8192
12	86093.9500	SO $v = 0$, $N_J = 2_2$–1_1	64	0.07 ∼ 0.84	⋯	⋯	8192
13	86243.3700	SiO $v = 1$, $J = 2$–1	64	0.07 ∼ 0.79	165 ∼ 384	0.05	8192
14	86846.9600	SiO $v = 0$, $J = 2$–1	64	0.06 ∼ 0.81	⋯	⋯	8192
15	88631.6023	HCN $v = 0$, $J = 1$–0	64	0.07 ∼ 0.75	⋯	⋯	8192
16	90771.5643	SiS $v = 0$, $J = 5$–4	64	0.07 ∼ 0.79	⋯	⋯	8192
17	128458.8872	SiO $v = 2$, $J = 3$–2	64	0.08 ∼ 0.81	⋯	⋯	8192
18	129363.2400	SiO $v = 1$, $J = 3$–2	64	0.07 ∼ 0.83	170 ∼ 593	0.036	8192
19	130268.6100	SiO $v = 0$, $J = 3$–2	64	0.08 ∼ 0.85	⋯	⋯	8192

with higher detectability rates; different characteristics in various SiO transition masers compared to M-type stars, especially the relatively high detection rates and intensity of the SiO $v = 2$, $J = 2$–1 maser; and kinematics associated with the acceleration mechanism from the atmosphere to the dust layer, H_2O maser, and thermal SiO envelope by measuring expansion velocities.

This paper presents source selection and observations in Section 2, observational results in Section 3, discussion of SiO $v = 2$, $J = 2$–1 detection rates, wind kinematics, and IRAS two-color diagram analysis in Section 4, and a summary in Section 5.

2. Source Selection and Observations

2.1. Source Selection

A total of 150 target sources for S-type stars were selected according to the following priorities. First, SiO maser-detected sources collected from the literature include A. Jorissen & G. R. Knapp (1998) and 10 in the SiO $v = 2$, $J = 2$–1 maser from V. Bujarrabal et al. (1996). Second, 19 SiO thermal-line detected sources were selected from S. Ramstedt et al. (2009). Third, CO-line detected sources include 21 from R. Sahai & S. Liechti (1995), seven from M. Andriantsaralaza et al. (2021), and seven from M. A. T. Groenewegen & T. de Jong (1998). Fourth, six sources detected in SiS or CS lines were selected from T. Danilovich et al. (2018). Fifth, we selected 19 sources from Spitzer spectroscopic survey results. Sixth, we also selected undetected sources from SiO and CO observational results listed in the first, second, and third priority groups. Additionally, 95 sources were selected from newly identified S-type stars by C. B. Stephenson (1984), P. S. Chen et al. (2019), and J. Chen et al. (2022). One extrinsic S-type star, W Aql, was included due to its interesting characteristics related to binary interactions (S. Ramstedt et al. 2017; T. Danilovich et al. 2021).

Table 1 presents the list of selected sources. In Columns (1) and (2), the source identification numbers and names are given, respectively. Columns (3) and (4) provide R.A. and decl. coordinates, indicating the position of each star. Columns (5) through (7) list the spectral type, stellar period, and stellar velocity ($V_\star$). Additionally, Columns (8) and (9) present the peak antenna temperatures of SiO $v = 1$, $J = 1$–0 and $v = 2$,

Table 3
HPBW, Aperture Efficiency and Conversion Factor

Site	Band (GHz)	HPBW (arcsec)	Aeff (%)	CF (Jy K^{-1})	Backend
(1)	(2)	(3)	(4)	(5)	(6)
KVNYS	22	130	65	12.21	DAS+DSM
	43	67	71	11.30	⋯
	43	67	72	11.10	⋯
	49	61	57	14.10	⋯
	86	32	54	14.90	⋯
	88	32	49	16.35	OCTAD+GSM
	90	31	53	14.96	⋯
	128	25	38	20.93	⋯
	130	25	37	21.76	⋯
KVNUS	22	129	69	11.58	DAS+DSM
	43	65	64	12.54	⋯
	43	67	65	11.40	⋯
	49	59	52	17.72	⋯
	86	32	67	15.45	⋯
	88	31	60	17.00	OCTAD+GSM
	90	31	67	15.36	⋯
	128	23	67	19.13	⋯
	130	23	46	19.12	⋯
KVNTN	22	128	70	11.40	DAS+DSM
	43	64	64	12.53	⋯
	43	68	64	12.45	⋯
	49	57	52	15.42	⋯
	86	31	59	13.47	⋯
	88	31	55	14.40	OCTAD+GSM
	90	31	58	13.78	⋯
	128	23	42	19.12	⋯
	130	22	42	18.91	⋯

Table 4
Detected Rate According to Observed Molecular Lines

Transition	Detections (Rates)
H_2O 6(1,6)–5(2,3)	⋯
SiO $v = 1$, $J = 3$–2	6 (4.00%)
SiO $v = 1$, $J = 2$–1	13 (8.66%)
SiO $v = 1$, $J = 1$–0	9 (6.00%)
SiO $v = 2$, $J = 3$–2	2 (1.33%)
SiO $v = 2$, $J = 2$–1	2 (1.33%)
SiO $v = 2$, $J = 1$–0	5 (3.33%)
SiO $v = 3$, $J = 1$–0	...
SiO $v = 0$, $J = 3$–2	7 (4.67%)
SiO $v = 0$, $J = 2$–1	6 (4.00%)
SiO $v = 0$, $J = 1$–0	5 (3.33%)
^{29}SiO $v = 0$, $J = 2$–1	1 (0.67%)
^{29}SiO $v = 0$, $J = 1$–0	2 (1.33%)
^{30}SiO $v = 0$, $J = 1$–0	...
HCN $v = 0$, $J = 1$–0	4 (2.67%)
SiS $v = 0$, $J = 5$–4	⋯
CS $v = 0$, $J = 1$–0	⋯
SO $v = 0$, $J = 2(2)$–1(1)	⋯
SO_2 $v = 0$, $J = 24_{(4,20)}$–$23_{(5,19)}$	⋯

Note. Detection rates (%) indicate the percentage of the number of detected sources among 150 observed sources.

$J = 2$–1 masers collected from the literature, with references provided in Column (10).

2.2. Observations

We performed observations toward 150 S-type AGB stars using the three KVN 21 m single-dish telescopes (KVN Yonsei telescope: KVNYS, KVN Ulsan telescope: KVNUS, and KVN Tamna telescope: KVNTN) from 2023 March to 2024 May. The upgraded KVN four wideband (22/43/86/129 GHz) receiving system was employed for simultaneous observations of H_2O and SiO multimaser lines together with several thermal lines, in total, nineteen molecular lines (Table 2). The frequency setting is same as SMASTES I for O-rich M-type stars (H. Baek et al. 2025), i. e., (K band) H_2O $6_{1,6}$–$5_{2,3}$ (22.235 GHz), SO_2 $v = 0$, $J_{K_a,K_c} = 24_{4,20}$–$23_{5,19}$ (22.483 GHz), (Q band) ^{28}SiO $v = 0$, 1, 2, 3, $J = 1$–0; ^{29}SiO $v = 0$, $J = 1$–0; ^{30}SiO $v = 0$, $J = 1$–0 (43.424, 43.122, 42.820, 42.519, 42.880, 42.373 GHz), CS $v = 0$, $J = 1$–0 (48.991 GHz), (W band) ^{28}SiO $v = 0$, 1, 2, $J = 2$–1; ^{29}SiO $v = 0$, $J = 2$–1 (86.847, 86.243, 85.640, 85.759 GHz), SO $v = 0$, $N_J = 2_2$–1_1 (86.094 GHz), HCN $v = 0$, $J = 1$–0 (88.632 GHz), SiS $v = 0$, $J = 5$–4 (90.772 GHz), and (D band) SiO $v = 0$, 1, 2, $J = 3$–2 (130.269, 129.363, 128.459 GHz), with a bandwidth of 64 MHz.

System noise temperatures ranged from 61 to 238 K at 22 GHz, 75 to 277 K at 43 GHz, 165 to 384 K at 86 GHz, and 170 to 593 K at 129 GHz, depending on weather conditions and source elevations. The backend system was also configured the same as in SMASTES I, providing a 64 MHz bandwidth that covers velocity ranges of 850 km s^{-1} (22 GHz), 440 km s^{-1} (43 GHz), 220 km s^{-1} (86 GHz), and 150 km s^{-1} (129 GHz). Corresponding velocity resolutions are 0.21 km s^{-1} (4096 channels at 22 GHz), 0.11 km s^{-1} (4096 channels at 43 GHz), 0.05 km s^{-1} (8192 channels at 86 GHz), and 0.036 km s^{-1} (8192 channels at 129 GHz). For consistency in detecting real signals, all four bands were smoothed to an effective resolution of ∼0.4 km s^{-1} in the final data reduction.

We adopted a position-switching mode with 1 minute ON/OFF integration per source. Pointing accuracy was checked every 2 hr using nearby strong SiO maser sources. The half-power beam widths (HPBW), aperture efficiencies, and conversion factors from antenna temperature (T_A^*) to flux density for the KVNYS, KVNUS, and KVNTN telescopes are summarized in Table 3 (KVN 2023 Status Report[4]).

Calibration was performed via the standard chopper-wheel method to correct for atmospheric attenuation and antenna gain variations with elevation, yielding spectra in terms of T_A^*. Typical on-source integration times were ∼100 minutes per source, achieving an rms noise level of 0.06–0.85 Jy. The average noise rms values for these observations were 0.18, 0.15, 0.27, and 0.39 Jy for the K, Q, W, and D bands, respectively, with an overall average of about 0.26 Jy indicating that the data set is consistent and uniform across the observed frequency bands. All data reduction was carried out using the Continuum and Line Analysis Single-dish Software package within the GILDAS[5] distribution.

3. Observational Results

Overall detected number of sources and their detection rates are given in Table 4 according to 19 observed molecular transitions. The SiO $v = 1$, $J = 1$–0, 2–1, and 3–2 masers were detected from nine, 13, and six sources among 150 S-type stars, corresponding to detection rates of 6.0%, 8.7%, and 4.0%, respectively. Among these, the SiO maser emission from T Sgr was detected for the first time. The SiO $v = 1$, $J = 2$–1 maser was detected in more stars than the $v = 1$, $J = 1$–0 maser, despite requiring a higher rotational excitation energy compared to that of the SiO $v = 1$, $J = 1$–0 maser. This trend is the same as in SRs of M-type O-rich stars (H. Baek et al. 2025). The detection rates of the SiO $v = 0$, $J = 1$–0, $J = 2$–1, and $J = 3$–2 lines (SiO ground vibrational state) increase toward a higher rotational transition from $J = 1$–0 to $J = 3$–2 like the trend in SRs and Miras of O-rich M-type stars (H. Baek et al. 2025). The SiO $v = 2$, $J = 2$–1 weak maser was detected from only 2 S-type stars, V418 Cas (#15) and χ Cyg (#114). It was the first detection from V418 Cas (#15). The $v = 2$, $J = 2$–1 maser was not detected in 4 S-type stars (S Cas (#16), W And (#21), ST Sgr (#100), and W Aql (#102)) with the 3σ levels of 0.09–1.39 Jy in which it was detected with IRAM 30 m telescope (V. Bujarrabal et al. 1996). The ^{29}SiO $v = 0$, $J = 1$–0 line was detected from S Cas (#16) and χ Cyg (#114), and the ^{29}SiO $v = 0$, $J = 2$–1 line was detected from χ Cyg (#114). The SiO $v = 3$, $J = 1$–0 maser and ^{30}SiO $v = 0$, $J = 1$–0 line were not detected. In particular, no H_2O maser has been detected in any S-type stars among 150 sources. HCN line was detected in 4 S-type stars; S Cas (#16), W Aql (#102), R Cyg (#110), and χ Cyg (#114). SiS, CS, SO, and SO_2 lines were not detected.

Tables 5–9 give the properties of the detected spectra according to source identification number. Tables 5 and 6 list the peak and integrated fluxes for 14 detected sources, respectively. Table 7 gives the peak and integrated flux density ratios with respect to the SiO $v = 1$, $J = 1$–0 maser and SiO $v = 1$, $J = 2$–1 maser. Tables 8 and 9 provide peak and mean velocities. Table 10 lists full width at zero power (FWZP) values.

[4] https://radio.kasi.re.kr/status_report.php
[5] https://www.iram.fr/IRAMFR/GILDAS/

Table 5
Peak Flux

NO.	Source Name	^{29}SiO $J = 1$–0	SiO $J = 1$–0			^{29}SiO $J = 2$–1	SiO $J = 2$–1			SiO $J = 3$–2			HCN
		$v = 0$	$v = 0$	$v = 1$	$v = 2$	$v = 0$	$v = 0$	$v = 1$	$v = 2$	$v = 0$	$v = 1$	$v = 2$	$v = 0$
(1)	(2)	(3)	(4)	(5)	(6)	(7)	(8)	(9)	(10)	(11)	(12)	(13)	(14)
6	R And	⋯	⋯	4.00	⋯	⋯	0.75	17.58	⋯	⋯	⋯	⋯	⋯
9	RW And	⋯	⋯	1.66	⋯	⋯	⋯	6.26	⋯	⋯	24.59	⋯	⋯
15	V418 Cas	⋯	⋯	0.78	⋯	⋯	⋯	1.79	1.34	⋯	⋯	⋯	⋯
16	S Cas	3.55	0.33	⋯	2.11	⋯	1.19	0.45	⋯	1.96	8.05	⋯	1.64
21	W And	⋯	⋯	20.20	6.88	⋯	1.19	39.04	⋯	1.52	25.68	4.40	⋯
83	RS Cnc	⋯	0.89	⋯	⋯	⋯	13.41	⋯	⋯	15.68	⋯	⋯	⋯
91	S Her	⋯	⋯	9.99	2.98	⋯	⋯	11.03	⋯	⋯	⋯	⋯	⋯
100	ST Sgr	⋯	0.89	0.99	⋯	⋯	⋯	23.61	⋯	⋯	18.49	⋯	⋯
102	W Aql (230911)	⋯	14.19	⋯	⋯	⋯	23.36	38.55	⋯	97.94	⋯	⋯	99.39
	W Aql (100116)	⋯	⋯	33.97	⋯	⋯	⋯	⋯	⋯	⋯	⋯	⋯	⋯
	W Aql (100515)	⋯	⋯	29.08	⋯	⋯	⋯	⋯	⋯	⋯	⋯	⋯	⋯
	W Aql (220106)	⋯	⋯	⋯	⋯	⋯	⋯	7.84	⋯	⋯	2.29	⋯	⋯
	W Aql (220302)	⋯	⋯	⋯	⋯	⋯	⋯	34.42	⋯	⋯	22.88	⋯	⋯
	W Aql (220510)	⋯	⋯	6.15	⋯	⋯	⋯	35.01	⋯	⋯	36.83	⋯	⋯
104	T Sgr	⋯	⋯	⋯	⋯	⋯	⋯	12.42	⋯	⋯	⋯	⋯	⋯
110	R Cyg	⋯	⋯	2.42	⋯	⋯	⋯	4.42	⋯	3.88	⋯	⋯	1.95
114	χ Cyg	3.75	5.88	6.05	4.42	14.93	23.51	15.96	14.97	83.54	7.03	5.05	11.15
126	V865 Aql	⋯	⋯	⋯	8.42	⋯	⋯	13.45	⋯	⋯	⋯	⋯	⋯
150	WY Cas	⋯	⋯	1.43	⋯	⋯	⋯	9.84	⋯	9.03	7.09	⋯	⋯

Note. Peak temperature measurements for various sources, showing the peak intensity in Kelvin (K) for different molecular transitions and vibrational states.

Table 6
Integrated Flux

NO.	Source Name	^{29}SiO $J = 1$–0	SiO $J = 1$–0			^{29}SiO $J = 2$–1	SiO $J = 2$–1			SiO $J = 3$–2			HCN
		$v = 0$	$v = 0$	$v = 1$	$v = 2$	$v = 0$	$v = 0$	$v = 1$	$v = 2$	$v = 0$	$v = 1$	$v = 2$	$v = 0$
(1)	(2)	(3)	(4)	(5)	(6)	(7)	(8)	(9)	(10)	(11)	(12)	(13)	(14)
6	R And	⋯	⋯	6.66	⋯	⋯	18.18	50.06	⋯	⋯	⋯	⋯	⋯
9	RW And	⋯	⋯	6.88	⋯	⋯	⋯	29.40	⋯	⋯	98.54	⋯	⋯
15	V418 Cas	⋯	⋯	4.22	⋯	⋯	⋯	10.28	2.68	⋯	⋯	⋯	⋯
16	S Cas	5.44	7.99	⋯	4.55	⋯	31.34	3.43	⋯	55.96	23.28	⋯	54.98
21	W And	⋯	⋯	108.56	22.87	⋯	5.81	236.91	⋯	27.66	126.91	1.67	⋯
83	RS Cnc	⋯	0.89	⋯	⋯	⋯	13.41	⋯	⋯	15.66	⋯	⋯	⋯
91	S Her	⋯	⋯	9.99	2.22	⋯	⋯	11.03	⋯	⋯	⋯	⋯	⋯
100	ST Sgr	⋯	0.11	0.99	⋯	⋯	⋯	91.78	⋯	⋯	44.84	⋯	⋯
102	W Aql (230911)	⋯	13.21	⋯	⋯	⋯	51.11	38.59	⋯	252.42	⋯	⋯	132.80
	W Aql (100116)	⋯	⋯	51.15	⋯	⋯	⋯	⋯	⋯	⋯	⋯	⋯	⋯
	W Aql (100515)	⋯	⋯	75.94	⋯	⋯	⋯	⋯	⋯	⋯	⋯	⋯	⋯
	W Aql (220106)	⋯	⋯	⋯	⋯	⋯	⋯	14.27	⋯	⋯	4.21	⋯	⋯
	W Aql (220302)	⋯	⋯	⋯	⋯	⋯	⋯	74.63	⋯	⋯	34.21	⋯	⋯
	W Aql (220510)	⋯	⋯	10.40	⋯	⋯	⋯	88.46	⋯	⋯	47.75	⋯	⋯
104	T Sgr	⋯	⋯	⋯	⋯	⋯	⋯	16.69	⋯	⋯	⋯	⋯	⋯
110	R Cyg	⋯	⋯	2.22	⋯	⋯	⋯	4.02	⋯	10.23	⋯	⋯	3.27
114	χ Cyg	3.44	7.33	6.22	2.33	22.30	23.64	23.24	16.24	121.59	23.07	3.35	7.85
126	V865 Aql	⋯	⋯	⋯	10.10	⋯	⋯	6.85	⋯	⋯	⋯	⋯	⋯
150	WY Cas	⋯	⋯	1.78	⋯	⋯	⋯	12.81	⋯	6.94	5.02	⋯	⋯

Note. Integrated intensities of different molecular transitions for various sources, multiplied by the appropriate factor, presented in K km s^{-1}.

For S-type stars, the average ratio of SiO $v = 1$, $J = 2$–1 to SiO $v = 1$, $J = 1$–0 is 13.11, whereas the corresponding values for SRs, Miras, and OH/IR objects from SMASTES I are 1.60, 1.02, and 1.07, respectively (H. Baek et al. 2025). This indicates that S-type stars exhibit a significantly larger high-excitation transition relative to the fundamental $J = 1$–0 transition. Likewise, the average ratio of SiO $v = 1$, $J = 3$–2 to SiO $v = 1$, $J = 1$–0 is 13.51 for the S-type sample, whereas the values reported for SRs, Miras, and OH/IR objects from SMASTES I are 0.42, 0.36, and 0.60, respectively (H. Baek et al. 2025). These comparisons suggest that excitation conditions in the extended atmospheres of S-type stars may differ substantially from those in other late-type variables.

No 16. S Cas. The SiO ($v = 1$, $J = 2-1$ and $J = 3-2$; $v = 2$, $J = 1-0$; ^{29}SiO $v = 0$, $J = 1-0$) maser lines were detected at about stellar velocity ($V_\star = -31$ km s^{-1}), which is the central velocity of SiO and HCN thermal lines. The lowest rotational transition maser of SiO $v = 1$, $J = 1-0$ was not detected

Table 7
Ratio of Peak and Integrated flux

NO.	Source Name	$\frac{\mathrm{P.F(SiO}\ v=1, J=2-1)}{\mathrm{P.F(SiO}\ v=1, J=1-0)}$	$\frac{\mathrm{P.F(SiO}\ v=1, J=3-2)}{\mathrm{P.F(SiO}\ v=1, J=1-0)}$	$\frac{\mathrm{P.F(SiO}\ v=1, J=3-2)}{\mathrm{P.F(SiO}\ v=1, J=2-1)}$	$\frac{\mathrm{I.F(SiO}\ v=1, J=2-1)}{\mathrm{I.F(SiO}\ v=1, J=1-0)}$	$\frac{\mathrm{I.F(SiO}\ v=1, J=3-2)}{\mathrm{I.F(SiO}\ v=1, J=1-0)}$	$\frac{\mathrm{I.F(SiO}\ v=1, J=3-2)}{\mathrm{I.F(SiO}\ v=1, J=2-1)}$
6	R And	4.39	⋯	⋯	7.52	⋯	⋯
9	RW And	3.77	14.81	3.93	4.27	14.32	3.35
15	V418 Cas	2.29	⋯	⋯	2.44	⋯	⋯
16	S Cas	⋯	⋯	17.89	⋯	⋯	6.79
21	W And	1.93	1.27	0.66	2.18	1.17	0.54
83	RS Cnc	⋯	⋯	⋯	⋯	⋯	⋯
91	S Her	1.1	⋯	⋯	1.10	⋯	⋯
100	ST Sgr	91.78	44.83	0.49	92.71	45.29	0.49
102	W Aql (230911)	⋯	⋯	⋯	⋯	⋯	⋯
	W Aql (220106)	⋯	⋯	0.29	⋯	⋯	0.29
	W Aql (220302)	⋯	⋯	0.66	⋯	⋯	0.46
	W Aql (220510)	⋯	⋯	1.05	⋯	⋯	0.54
104	T Sgr	⋯	⋯	⋯	⋯	⋯	⋯
110	R Cyg	1.81	⋯	⋯	1.81	⋯	⋯
114	χ Cyg	3.74	3.71	0.99	3.74	3.71	0.99
126	V865 Aql	⋯	⋯	⋯	⋯	⋯	⋯
150	WY Cas	7.2	2.93	0.41	7.20	2.82	0.39

Note. The combined ratios of integrated intensities from two data sets.

Table 8
Peak Velocity

NO.	Source Name	^{29}SiO $J=1$–0	SiO $J=1$–0			^{29}SiO $J=2$–1	SiO $J=2$–1			SiO $J=3$–2			HCN
		$v=0$	$v=0$	$v=1$	$v=2$	$v=0$	$v=0$	$v=1$	$v=2$	$v=0$	$v=1$	$v=2$	$v=0$
(1)	(2)	(3)	(4)	(5)	(6)	(7)	(8)	(9)	(10)	(11)	(12)	(13)	(14)
6	R And	⋯	⋯	−13.3	⋯	⋯	−15.3	−16.0	⋯	⋯	⋯	⋯	⋯
9	RW And	⋯	⋯	−7.6	⋯	⋯	⋯	−2.8	⋯	⋯	−8.1	⋯	⋯
15	V418 Cas	⋯	⋯	−12.4	⋯	⋯	⋯	−17.6	−13.9	⋯	⋯	⋯	⋯
16	S Cas	−30.9	−31.7	⋯	−32.3	⋯	−32.1	−31.7	⋯	−29.5	−33.0	⋯	−28.8
21	W And	⋯	⋯	−38.0	−39.5	⋯	−33.4	−37.6	⋯	−35.0	−36.3	−36.3	⋯
83	RS Cnc	⋯	5.5	⋯	⋯	⋯	9.0	⋯	⋯	6.2	⋯	⋯	⋯
91	S Her	⋯	⋯	4.7	4.2	⋯	⋯	2.5	⋯	⋯	⋯	⋯	⋯
100	ST Sgr	⋯	52.5	56.4	⋯	⋯	⋯	52.7	⋯	⋯	53.1	⋯	⋯
102	W Aql (230911)	⋯	−29.1	⋯	⋯	⋯	−22.6	−22.2	⋯	−19.8	⋯	⋯	−25.7
	W Aql (100116)	⋯	⋯	−23.9	⋯	⋯	⋯	⋯	⋯	⋯	⋯	⋯	⋯
	W Aql (100515)	⋯	⋯	−24.8	⋯	⋯	⋯	⋯	⋯	⋯	⋯	⋯	⋯
	W Aql (220106)	⋯	⋯	⋯	⋯	⋯	⋯	−24.1	⋯	⋯	−23.9	⋯	⋯
	W Aql (220302)	⋯	⋯	⋯	⋯	⋯	⋯	−24.0	⋯	⋯	−24.1	⋯	⋯
	W Aql (220510)	⋯	⋯	−23.5	⋯	⋯	⋯	−23.7	⋯	⋯	−23.9	⋯	⋯
104	T Sgr	⋯	⋯	⋯	⋯	⋯	⋯	5.2	⋯	⋯	⋯	⋯	⋯
110	R Cyg	⋯	⋯	−14.5	⋯	⋯	⋯	−16.8	⋯	−17.7	⋯	⋯	−18.8
114	χ Cyg	9.6	9.8	8.9	9.5	9.6	9.5	8.5	9.0	11.5	10.6	10.1	9.8
126	V865 Aql	⋯	⋯	⋯	37.4	⋯	⋯	37.9	⋯	⋯	⋯	⋯	⋯
150	WY Cas	⋯	⋯	12.1	⋯	⋯	⋯	11.2	⋯	9.7	12.0	⋯	⋯

Note. Peak velocity measurements for various sources, presented in km s^{-1}.

although the $v=1$, $J=2-1$ and $J=3-2$ masers were detected. The ground-state emission of SiO $v=0$ shows stronger intensity as the rotational transition increases from $J=1-0$ to $J=3-2$. The SiO $v=2$, $J=2-1$ maser was detected from this source by IRAM 30 m telescope (V. Bujarrabal et al. 1996), but not in this observation. Mass-loss rates were estimated to be $3.5\times10^{-6}M_{\odot}$ and $2.8\times10^{-6}M_{\odot}$ by S. Ramstedt et al. (2009) and T. Danilovich et al. (2018), which is high compared to the mass-loss rates of other S-type stars. Also, the SiO expansion velocities measured by a half of FWZPs of SiO $v=0$, $J=2-1$ and $J=3-2$ lines (28.6 km s^{-1} by SiO $v=0$, $J=2-1$, 30.3 km s^{-1} by SiO $v=0$, $J=3-2$; Table 9) were larger than those (19 km s^{-1} and 20.5 km s^{-1}) by S. Ramstedt et al. (2009) and T. Danilovich et al. (2018).

No 21. W And. The SiO $v=1$, $J=1-0$, $J=2-1$, and $J=3-2$ masers were all detected. The peak intensity of the $v=1$, $J=2-1$ maser (39.04 Jy) is stronger than that of the $v=1$, $J=1-0$ maser (20.20 Jy). The SiO $v=2$, $J=3-2$ maser was detected, but the $v=2$, $J=2-1$ maser was not detected. With the IRAM 30 m telescope, the $v=2$, $J=2-1$ maser was detected at −37.5 km s^{-1} with an intensity of 0.4 Jy (V. Bujarrabal et al. 1996). The peak velocities of SiO $v=1$, $J=1-0$, $J=2-1$, and $J=3-2$ masers show blueshifted emission with respect to the stellar velocity of −35 km s^{-1}. Mass-loss rates were estimated to be $1.7\times10^{-7}M_{\odot}$ and $2.8\times10^{-7}M_{\odot}$

Table 9
Mean Velocity

NO.	Source Name	^{29}SiO $J=1$–0	SiO $J=1$–0			^{29}SiO $J=2$–1	SiO $J=2$–1			SiO $J=3$–2			HCN
		$v=0$	$v=0$	$v=1$	$v=2$	$v=0$	$v=0$	$v=1$	$v=2$	$v=0$	$v=1$	$v=2$	$v=0$
(1)	(2)	(3)	(4)	(5)	(6)	(7)	(8)	(9)	(10)	(11)	(12)	(13)	(14)
6	R And	⋯	⋯	−13.9	⋯	⋯	−12.2	−15.3	⋯	⋯	⋯	⋯	⋯
9	RW And	⋯	⋯	−6.3	⋯	⋯	⋯	−4.8	⋯	⋯	−6.6	⋯	⋯
15	V418 Cas	⋯	⋯	−12.0	⋯	⋯	⋯	−17.1	−13.7	⋯	⋯	⋯	⋯
16	S Cas	−31.0	−31.5	⋯	−31.6	⋯	−32.3	−33.1	⋯	−29.5	−31.7	⋯	−28.9
21	W And	⋯	⋯	−37.4	−41.5	⋯	−33.6	−36.7	⋯	−34.7	−36.4	−36.5	⋯
83	RS Cnc	⋯	8.0	⋯	⋯	⋯	6.9	⋯	⋯	7.4	⋯	⋯	⋯
91	S Her	⋯	⋯	2.5	4.0	⋯	⋯	0.5	⋯	⋯	⋯	⋯	⋯
100	ST Sgr	⋯	53.9	56.0	⋯	⋯	⋯	55.3	⋯	⋯	53.1	⋯	⋯
102	W Aql (230911)	⋯	−36.4	⋯	⋯	⋯	−26.7	−22.5	⋯	−18.8	⋯	⋯	−24.7
	W Aql (100116)	⋯	⋯	−23.5	⋯	⋯	⋯	⋯	⋯	⋯	⋯	⋯	⋯
	W Aql (100515)	⋯	⋯	−23.9	⋯	⋯	⋯	⋯	⋯	⋯	⋯	⋯	⋯
	W Aql (220106)	⋯	⋯	⋯	⋯	⋯	⋯	−23.3	⋯	⋯	−23.9	⋯	⋯
	W Aql (220302)	⋯	⋯	⋯	⋯	⋯	⋯	−23.1	⋯	⋯	−23.7	⋯	⋯
	W Aql (220510)	⋯	⋯	−22.4	⋯	⋯	⋯	−22.4	⋯	⋯	−22.5	⋯	⋯
104	T Sgr	⋯	⋯	⋯	⋯	⋯	⋯	6.4	⋯	⋯	⋯	⋯	⋯
110	R Cyg	⋯	⋯	−13.6	⋯	⋯	⋯	−16.5	⋯	−16.6	⋯	⋯	−17.5
114	χ Cyg	8.3	8.7	8.2	8.6	9.5	9.1	8.1	8.6	9.0	7.5	8.9	8.7
126	V865 Aql	⋯	⋯	⋯	38.1	⋯	⋯	38.9	⋯	⋯	⋯	⋯	⋯
150	WY Cas	⋯	⋯	12.1	⋯	⋯	⋯	11.2	⋯	8.3	11.7	⋯	⋯

Note. Mean velocity measurements for various sources, presented in km s^{-1}.

by S. Ramstedt et al. (2009) and T. Danilovich et al. (2018) using the terminal velocity of 6 km s^{-1} based on CO observation (S. Ramstedt et al. 2009).

No 102. W Aql. This star is a binary star as extrinsic S-type AGB star (S. Ramstedt et al. 2011). Only the SiO $v=1$, $J=2-1$ maser was detected showing a redshifted emission with respect to the stellar velocity (−26 km s^{-1}). The SiO $v=1$, $v=2$, $J=1-0$ masers were detected at −23.7 and −24.7 km s^{-1} with peak temperatures of 32.5 Jy (2.77 K) and 0.9 Jy (0.08 K) by S.-H. Cho & J. Kim (2012). Figure 1 shows 2 epoch data in 2010 and 3 epoch data in 2022 for this stars together with 230911 data. The SiO $v=1$, $J=3-2$ maser was detected in these three epochs together with the $v=1$, $J=2-1$ maser but the $v=1$, 2, $J=1-0$ masers were not detected on 2022 January 6 and March 2. However, the SiO $v=1$, $J=1-0$ maser was detected on 2022 May 10 (∼0.5 K). S. Ramstedt et al. (2012) did not also detect these masers during several epochs in 2011. Long-term monitoring observational studies are required to investigate the reason why these masers disappear or reappear. The SiO $v=0$, $J=1-0$, $J=2-1$, and $J=3-2$ lines show stronger intensity as the rotational transition increases from $J=1-0$ to $J=3-2$. E. De Beck & H. Olofsson (2020) concluded that circumstellar environment of W Aql appears considerably closer to that of a C-type star than to that in unbiased observations of 159–211 GHz with the APEX. By ALMA observations, T. Danilovich et al. (2021) found that AlCl comes from a clump within 0.″1 very close to the star, while the AlF is more extended.

No 114. χ Cyg. The SiO $v=1$, $J=1-0$, $J=2-1$, and $J=3-2$ masers were detected around the stellar velocity of 9 km s^{-1} showing the strongest peak intensity of ∼15.96 Jy in the SiO $v=1$, $J=2-1$ maser. The SiO $v=2$, $J=2-1$ maser shows a spike feature on a smooth plateau component unlike other $v=2$, $J=2-1$ masers (V. Bujarrabal et al. 1996). The SiO $v=0$, $J=1-0$, $J=2-1$, and $J=3-2$ lines were detected and the $v=0$, $J=1-0$ line shows a spike maser feature on a wide plateau. P. De Vicente et al. (2016) checked the time variability of the $v=0$, $J=1-0$ line for a period longer than a year and reported that the spike was significantly varied. The ^{29}SiO $v=0$, $J=1-0$ line shows typical maser feature with a narrow spike. The HCN $v=0$, $J=1-0$ line exhibits three spikes on the top of pedestal showing a maser feature. Using the NOEMA array, D. T. Hoai et al. (2024) has reported that a bright HCN $J=3$–2 line is confined very close to the central star and is more widely distributed in 2024 than in 2023. They interpreted such variability in terms of maser emission.

4. Discussion

4.1. Low Detection Rate of the SiO v = 2, J = 2–1 Maser

The SiO $v=2, J=2$–1 maser would be expected to have some degree of detection from S-type stars where 22 GHz H_2O maser is not detected. It is due to the IR line overlap effect between the $v=1$, $J=0\rightarrow v=2$, $J=1$ line of ^{28}SiO and the $v_2=0, 12_{7,5}\rightarrow v_2=1, 11_{6,6}$ line of H_2O by H. Olofsson et al. (1981, 1985). These overlaps can disrupt the pumping pathway for the $v=2, J=2$–1 transition in M-type stars that commonly exhibit H_2O maser. However, the SiO $v=2, J=2-1$ maser was detected only in two S-type stars (V418 Cas (#15), χ Cyg (#114)) with KVN and not detected in 4 S-type stars (S Cas (#16), W And (#21), ST Sgr (#100), and W Aql (#102)) in which this maser was detected with IRAM 30 m telescope (V. Bujarrabal et al. 1996). Table 11 shows an observational comparison of the SiO $v=2$ masers detected by the IRAM 30 m telescope but not by KVN.

As shown in Table 11, the 3σ levels of KVN observations are better than or similar to those of IRAM observations 6 Jy, except for the W And case. Therefore, nondetections of S Cas, ST Sgr, and W Aql appear to be due to intensity variations according to the phases of each pulsation cycle rather than

Table 10
FWZP

NO.	Source Name	^{29}SiO $J=1$–0	SiO $J=1$–0			^{29}SiO $J=2$–1	SiO $J=2$–1			SiO $J=3$–2			HCN	CO(1–0)
		$v=0$	$v=0$	$v=1$	$v=2$	$v=0$	$v=0$	$v=1$	$v=2$	$v=0$	$v=1$	$v=2$	$v=0$	
(1)	(2)	(3)	(4)	(5)	(6)	(7)	(8)	(9)	(10)	(11)	(12)	(13)	(14)	(15)
6	R And	⋯	⋯	8.5	⋯	⋯	37.5	11.6	⋯	⋯	⋯	⋯	⋯	16.0[1]
9	RW And	⋯	⋯	23.2	⋯	⋯	⋯	16.2	⋯	⋯	⋯	11.3	⋯	⋯
15	V418 Cas	⋯	⋯	56.4	⋯	⋯	⋯	13.9	6.2	⋯	⋯	⋯	⋯	⋯
16	S Cas	7.8	40.7	⋯	7.0	⋯	46.8	14.7	⋯	57.1	9.0	⋯	54.7	41.0[2]
21	W And	⋯	⋯	24.7	13.6	⋯	19.5	16.1	⋯	25.5	16.4	4.1	⋯	12.0[1]
83	RS Cnc	⋯	19.2	⋯	⋯	⋯	16.1	⋯	⋯	10.2	⋯	⋯	⋯	16.0[3]
91	S Her	⋯	⋯	17.8	9.3	⋯	⋯	9.6	⋯	⋯	⋯	⋯	⋯	⋯
100	ST Sgr	⋯	16.1	9.3	⋯	⋯	⋯	20.4	⋯	⋯	8.2	⋯	⋯	18.7[4]
102	W Aql (230911)	⋯	46.0	⋯	⋯	⋯	45.2	10.8	⋯	52.3	⋯	⋯	40.4	34.4[2]
	W Aql (100116)	⋯	⋯	6.5	⋯	⋯	⋯	⋯	⋯	⋯	⋯	⋯	⋯	⋯
	W Aql (100515)	⋯	⋯	8.4	⋯	⋯	⋯	⋯	⋯	⋯	⋯	⋯	⋯	⋯
	W Aql (220106)	⋯	⋯	⋯	⋯	⋯	⋯	6.5	⋯	⋯	5.9	⋯	⋯	⋯
	W Aql (220302)	⋯	⋯	⋯	⋯	⋯	⋯	7.1	⋯	⋯	6.2	⋯	⋯	⋯
	W Aql (220510)	⋯	⋯	5.5	⋯	⋯	⋯	11.24	⋯	⋯	6.12	⋯	⋯	⋯
104	T Sgr	⋯	⋯	⋯	⋯	⋯	⋯	13.1	⋯	⋯	⋯	⋯	⋯	20.6(2–1)[5]
110	R Cyg	⋯	⋯	8.7	⋯	⋯	⋯	7.7	⋯	22.2	⋯	⋯	20.6	18.0[2]
114	χ Cyg	11.7	21.5	11.6	5.5	25.1	25.6	8.2	19.4	25.8	13.1	7.0	24.4	17.0[2]
126	V865 Aql	⋯	⋯	⋯	10.1	⋯	⋯	14.3	⋯	⋯	⋯	⋯	⋯	⋯
150	WY Cas	⋯	⋯	4.6	⋯	⋯	⋯	13.1	⋯	29.9	5.7	⋯	⋯	27.0[2]

Note. FWZP measurements for various sources. The columns represent different molecular transitions and vibrational states, including the newly added CO(1–0) column. (1) T. Danilovich et al. (2015); (2) S. Ramstedt et al. (2009); (3) Y. Libert et al. (2010); (4) J. H. Bieging & W. B. Latter (1994); (5) M. Andriantsaralaza et al. (2021).

sensitivity. However, the W And case requires observations with higher sensitivity, as the KVN 3σ level is higher.

In the IRAS two-color diagram (Section 4.3), the SiO $v=2, J=2$–1 maser-detected sources, χ Cyg (#114) and V418 Cas (#15) are located in region I and region IIIa showing O-rich circumstellar shells. In addition, 4 SiO $v=2, J=2-1$ maser-detected sources from O-rich M-type stars (SMASTES I; H. Baek et al. 2025) are marked with a: NV Aur, b: TX Cam, c: IU Tau, d: V1111 Oph. The b: TX Cam and d: V1111 Oph are located in lower part of region VII with C-rich circumstellar shells. In the observations of SMASTES I, H_2O maser was not detected from TX Cam and IU Tau and detected from NV Aur (peak flux = 0.61 Jy) and V1111 Oph (peak flux = 2.1 Jy). Future investigation is needed regarding the detectability and pumping mechanism of the SiO $v=2, J=2$–1 maser including the IR line overlap effect between SiO and H_2O.

4.2. Wind Kinematics for Four HCN Detected Sources

We investigate the wind velocity profile based on simultaneously obtained KVN data as L. Decin et al. (2010) deduced in the O-rich star IK Tau. These observed data can provide the velocity structure associated with the acceleration process from the atmosphere of SiO maser regions to the dust layer, thermal SiO and HCN envelopes by measuring their expansion velocities for four HCN detected S-type stars (S Cas (#16), W Aql (#102), R Cyg (#110), and χ Cyg (#114)). The wind velocity profile of O-rich M-type stars was investigated for 11 HCN detected sources (H. Baek et al. 2025). Figure 2 shows expansion velocities according to radial extent from the central star. Each expansion velocity was measured by half of the FWZPs of each molecular line emitted from different radial regions. The expansion velocities of SiO maser regions inside the dust layer (located at 2–4 $R_\star$; P. J. Diamond et al. 1994; D. A. Boboltz & M. Wittkowski 2005) are estimated by the average value deduced from SiO $v=1, J=1$–$0, J=2$–1, and $J=3$–2 maser lines for masers detected more than two transitions. The expansion velocity above dust layer using H_2O maser could not be estimated because of nondetection. For angular extents of HCN and SiO thermal lines, we adopt observational results of the high-sensitivity ALMA S. H. J. Wallström et al. (2024). S. H. J. Wallström et al. (2024) measured the radial extents of HCN to be 22–590 $R_\star$ and that of SiO to be 140–1100 $R_\star$. We use their median values of HCN (120 $R_\star$) and SiO (440 $R_\star$) in Figure 3. HCN molecule is formed in the inner envelope due to non-equilibrium shock chemistry (D. Duari et al. 1998) and distributed further inside than SiO. The median value of CO radial extent is used to be 1300 $R_\star$. Existing CO data from the literature is used at terminal wind velocities.

The trend of velocity profile for four HCN detected S-type stars is similar to that for 11 HCN detected M-type O-rich stars. Figure 2 also shows that expansion velocity increases rapidly through the dust layer (due to radiation pressure on dust) and reaches mass-loss velocities (CO expansion velocities). The expansion velocities of HCN by half of the

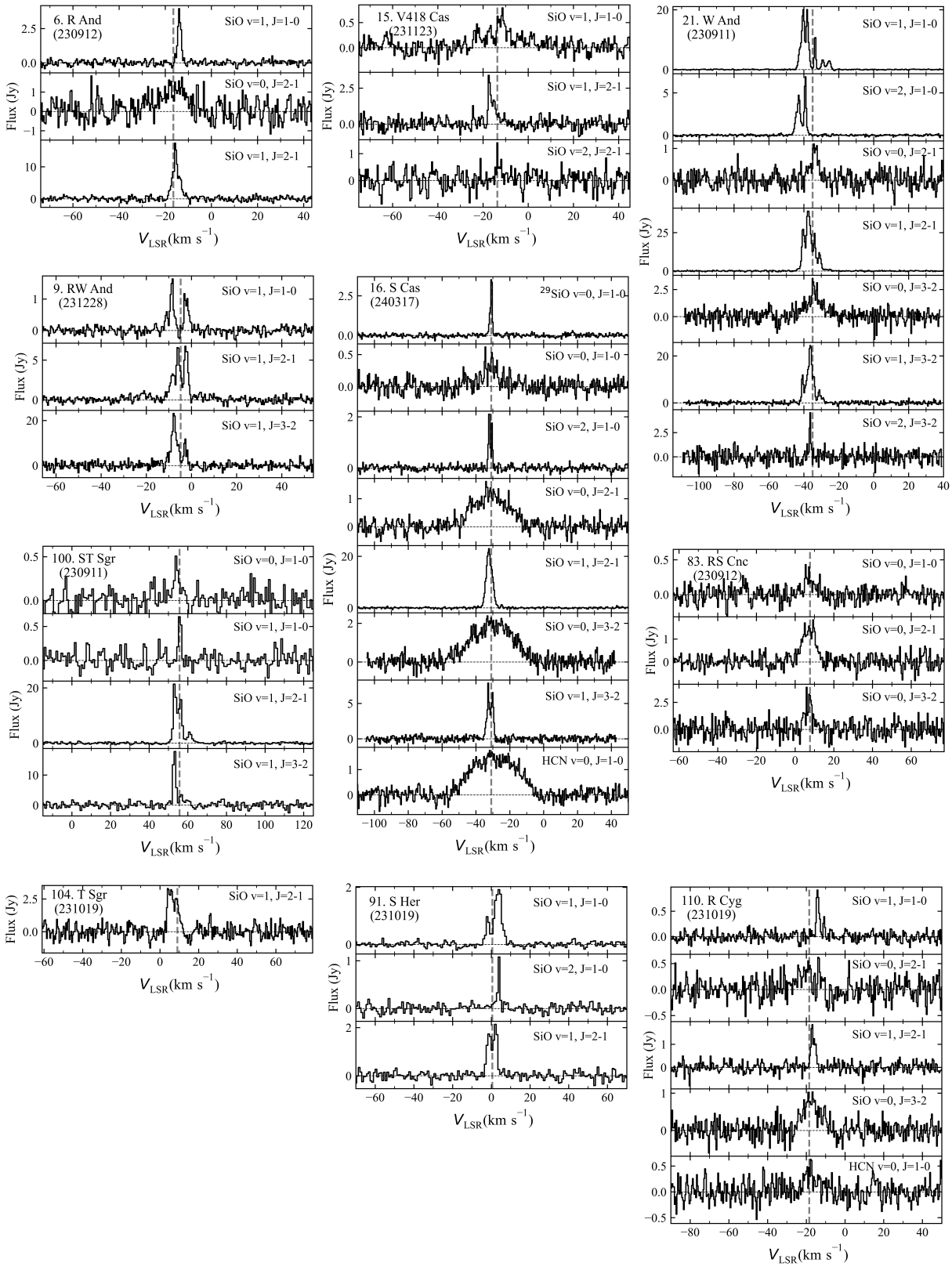

Figure 1. The spectra of 14 detected S-type stars observed from simultaneous observations of 19 molecular lines. The *X*-axis indicates the velocity of the local standard of rest (V_{LSR}), and the *Y*-axis indicates the flux density. The vertical gray solid line marks the stellar velocity. Additionally, spectra of W Aql observed with KVN from 2010 to 2022 are included, displaying five detected epochs. Observational dates are presented in yymmdd format, and the corresponding pulsation phase at each epoch is labeled as ϕ. The pulsation phases were calculated using available optical data from the American Association of Variable Star Observers (AAVSO; https://www.aavso.org).

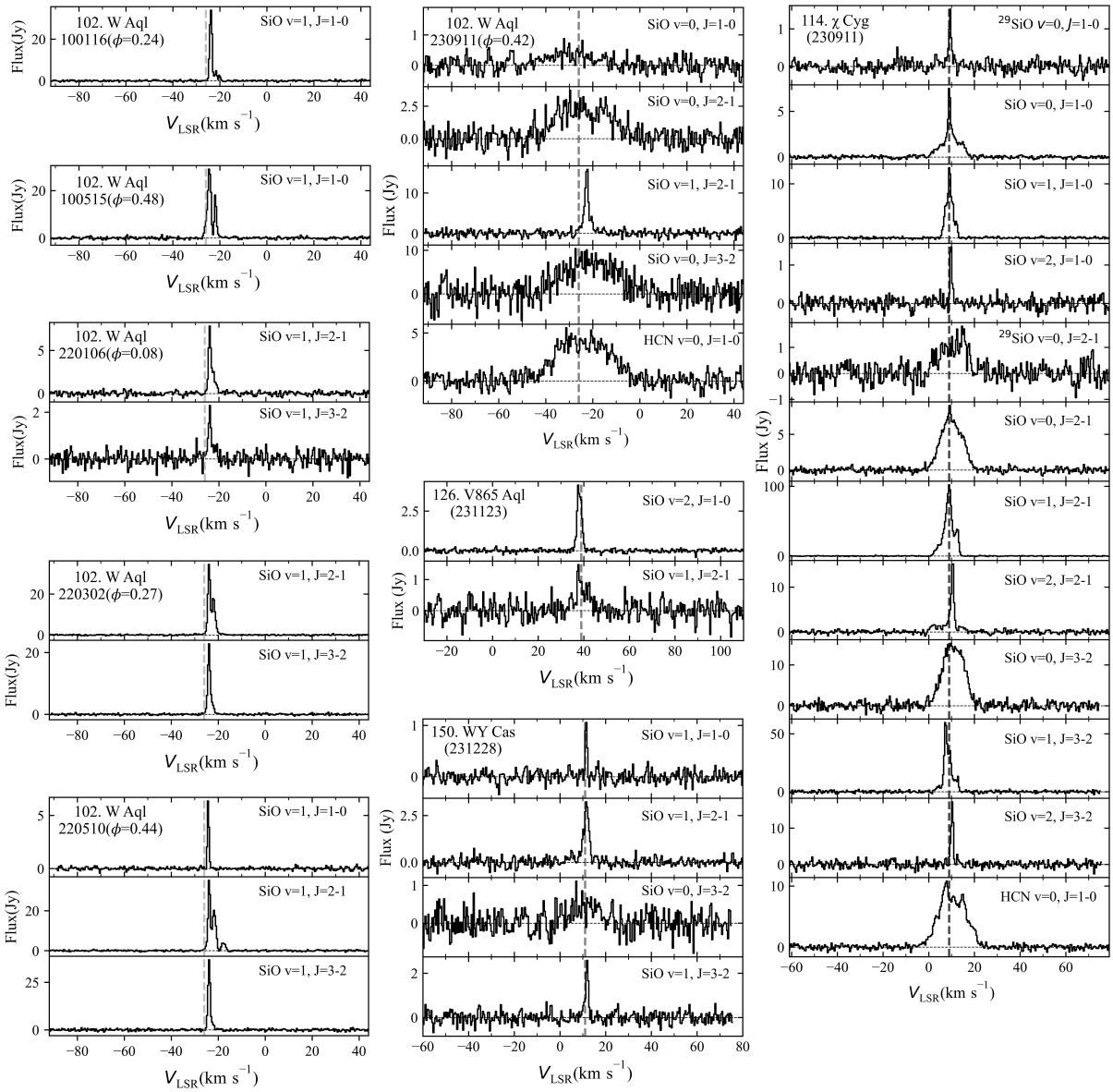

Figure 1. (Continued.)

Table 11
Comparison of Undetected Sources in KVN

Sources ($v = 2$, $J = 2$ −1 det.)	Flux (Jy) (IRAM 30m)	3σ levels (Jy) (KVN 21m)	ϕ (IRAM Obs)	ϕ (KVN Obs)
S Cas	2.3^h	0.09	0.01	0.92
W And	0.4*	1.39	0.42	0.08
ST Sgr	2.8^h	0.40	0.31	0.23
W Aql	9.8^h	0.89	0.43	0.42

Note. h means higher than 3σ levels of KVN 21 m observations. * indicates tentative detection. The 3σ levels of IRAM 30 m observations were 0.6 Jy for these four sources (V. Bujarrabal et al. 1996). ϕ: stellar optical phase.

FWZPs are larger compared to those of CO data like the case in 11 HCN detected M-type stars. It is likely due to the hyperfine splitting of the rotational levels in the HCN molecule.

These four HCN detected stars show different velocity profiles. For individual star, S Cas with the highest mass-loss rate shows the most rapid acceleration past the dust layer (from SiO maser region to HCN region) from 7.4 km s^{-1} to 26.9 and χ Cyg shows the most slow acceleration from 3.8 to 10.1. It is not easy to explain the different acceleration rate among four HCN detected S-type stars, although four S-type stars have different pulsation period and dust properties as Mira-type variables. I. McDonald & A. A. Zijlstra (2016) revealed that both pulsation period and amplitude are strongly correlated with dust emission, and that pulsation is the main trigger of mass loss. Anyway, this acceleration region plays an important role for initiating the mass loss as shown by the Pulsation-Enhanced Dust-Driven Outflow scenario (B. Freytag & S. Höfner 2008; S. Höfner et al. 2016; S. Höfner & H. Olofsson 2018).

In addition, as shown in Figure 2, CO expansion velocities of 4 HCN detected S-type stars show a smaller value than not only HCN expansion velocities but also SiO expansion

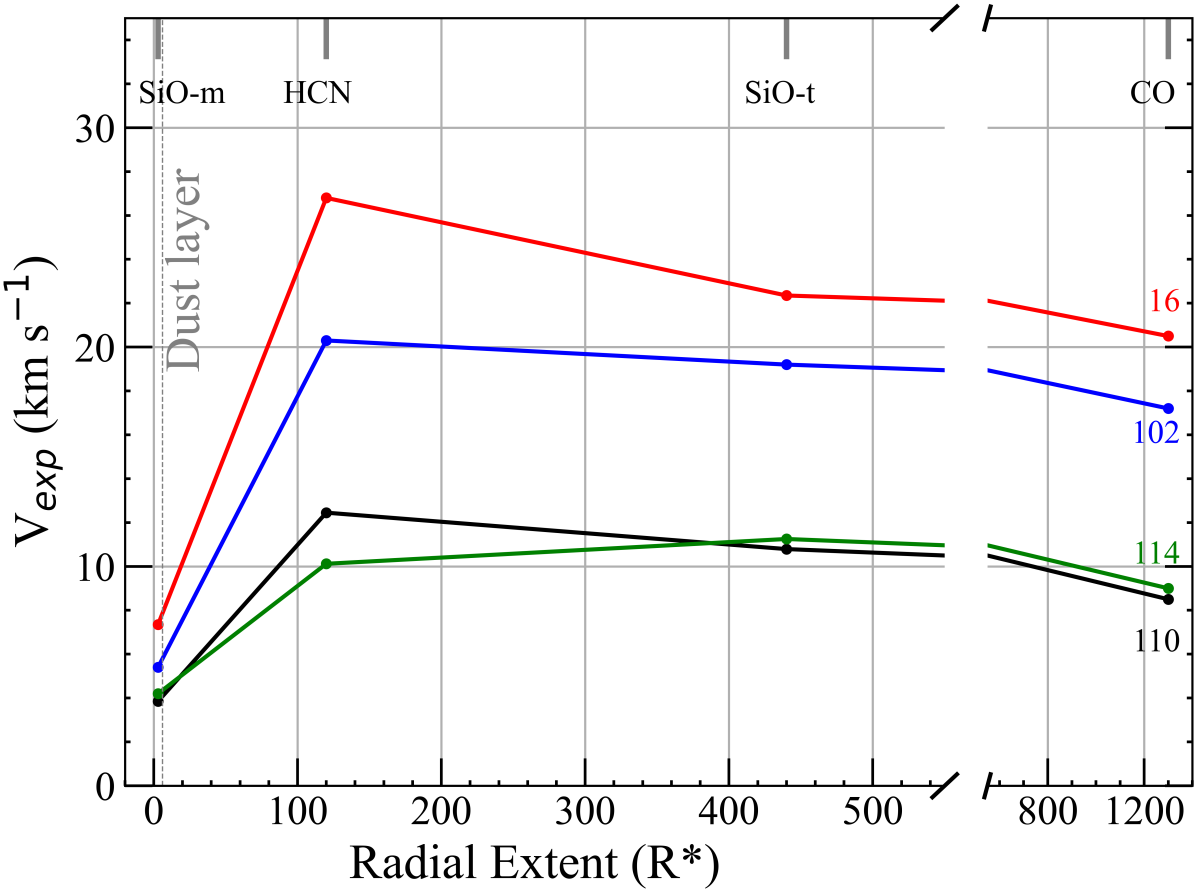

Figure 2. Wind velocity profile according to radial distances for 4 HCN detected S-type stars: S Cas (16), W Aql (102), R Cyg (110), and χ Cyg (114). The distances of the dominant line formation region in units of stellar radius from the central star are as follows. SiO maser adopted 3 R_* as the median value between 2 and 4 R_* (P. J. Diamond et al. 1994; D. A. Boboltz & M. Wittkowski 2005), and 120 R_* for HCN, 440 R_* for the SiO thermal lines, and 1300 R_* for CO lines based on the median values measured by S. H. J. Wallström et al. (2024). The vertical dashed line indicates dust condensation radius, $R_{\rm dust}$ at $\sim$6 R_* derived by C. A. Gottlieb et al. (2022b).

velocities. As the compact ATOMIUM CO ($v = 0$, $J = 2-1$) data showed (C. A. Gottlieb et al. 2022b), if S-type stars are observed with high-sensitivity ALMA, measured CO expansion velocities will be also 1.2–2 times larger than known CO expansion velocities in Table 10. However, the SiO and HCN expansion velocities would be measured to be a similar proportion larger than CO expansion velocities. Therefore, radial velocity curves in Figure 2 could be explained by a binary interaction with a (sub)stellar companion, rather than by the momentum equation for a spherical wind structure, as C. A. Gottlieb et al. (2022b) proposed. Also, the acceleration rate of the W Aql exceeds that of χ Cyg. It is not clear whether this is due to the impact of binary companions on the wind dynamics discussed by C. A. Gottlieb et al. (2022b). Velocity profiles of S-type stars can be compared with those of O-rich M-type stars (H. Baek et al. 2025) in relation to the facts that the wind acceleration by radiation pressure on dust are strongly affected by the C/O ratio (S. Höfner & H. Olofsson 2018).

4.3. Location of Maser and Thermal-line Detected Sources in IRAS Two-color Diagram

Figure 3 shows the location of 150 observed S-type AGB stars in IRAS two-color diagram (W. E. C. J. Van der Veen & H. J. Habing 1988). Fourteen SiO maser and thermal-line detected sources are distributed in O-rich star regions I, II, IIIa, and VII (C-rich star region) near the O-rich star region. Nondetected S-type stars are distributed in regions VIa (mainly C-rich) and VIb (some O-rich). In the case of O-rich M-type stars (SMASTES I), SiO and/or H_2O maser-detected sources are mainly distributed in regions II, IIIa, and IIIb, which are variable star regions with O-rich circumstellar shells.

Here we can try to explain these distributions by adopting an evolutionary sequence of S-type stars from O-rich M-type stars to a carbon star. The SiO and H_2O maser lines might depend upon C/O ratios and the development of circumstellar shells. Dredge-up of carbon from He-shell burning in O-rich AGB stars plays an important role in the chemical evolution from O-rich M-type stars to carbon stars (I. Iben & A. Renzini 1983; F. Herwig 2005) and changes the spectral type, M $\rightarrow$ MS $\rightarrow$ S $\rightarrow$ SC $\rightarrow$ C, depending on C/O ratio changes, including an increase in the abundance of s-process elements (A. D. Vanture et al. 2002). MS and SC stars are slightly lower and slightly larger values centered on C/O $\simeq$ 1. As the C/O ratio increases more and more, O-bearing masers such as SiO or H_2O can either vanish or be severely weakened.

Considering the high density of SiO maser conditions, the sources with SiO masers could be classified as MS or S type rather than SC type, since MS or S stars have enough SiO in

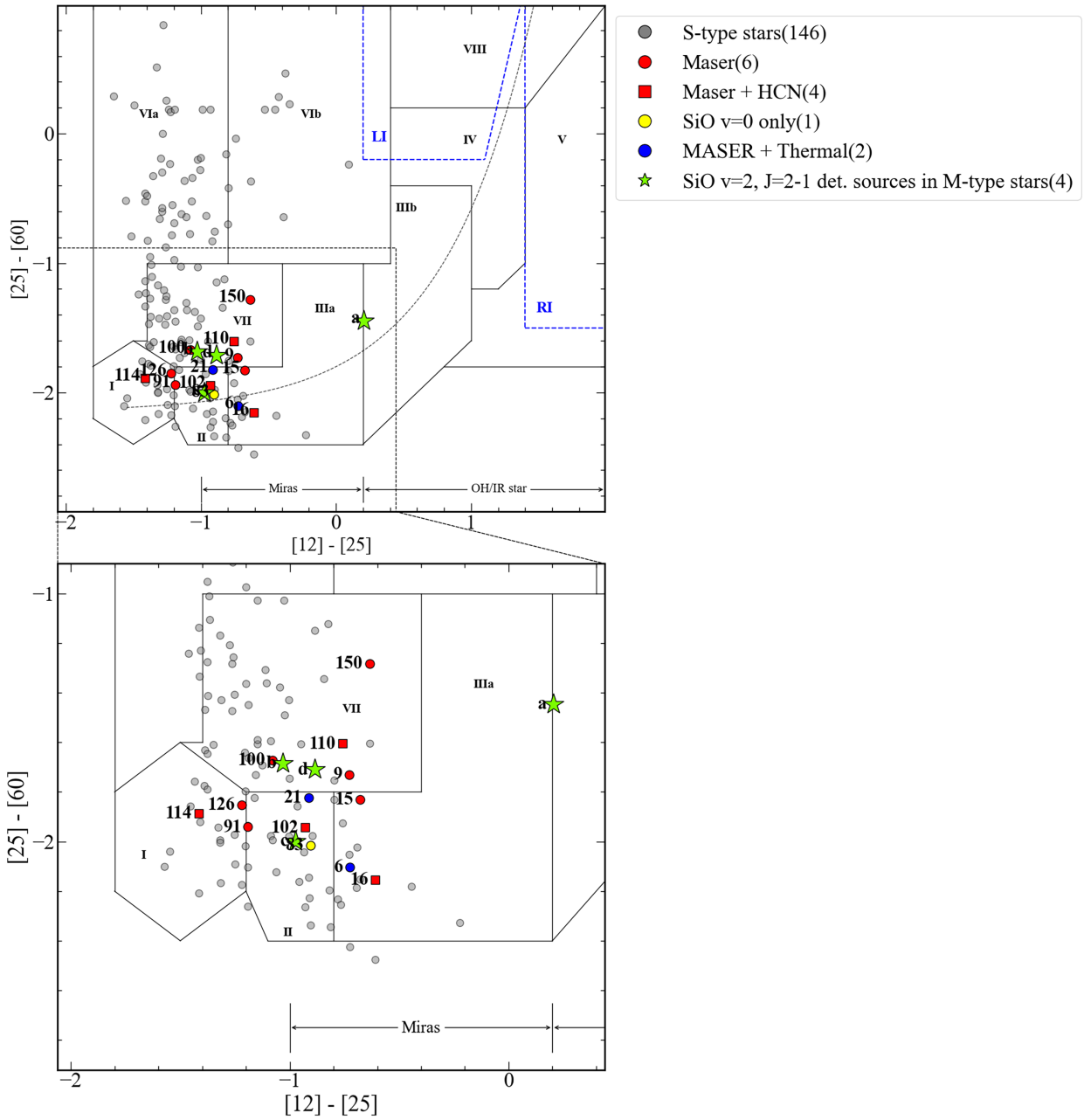

Figure 3. Observational results of S-type stars in the IRAS Two-color diagram for 146 stars with available IRAS data. The curved black solid line is the evolutionary track defined by W. E. C. J. Van der Veen & H. J. Habing (1988). The blue dashed line indicates the two groups of post-AGB stars, LI (left of IRAS; blue group) and RI (right of IRAS; red group; M. N. Sevenster 2002b). Gray circles indicate S-type stars in which no maser or thermal lines were detected. Red circles indicate (9: RW And, 15: V418 Cas, 91: S Her, 100: ST Sgr, 126: V865 Aql, 150: WY Cas), red rectangles SiO and HCN detected sources (16: S Cas, 102: W Aql, 110: R Cyg, 114: χ Cyg). Yellow circle (83: RS Cnc) and blue circles (6: R And, 21: W And). Green stars mark M-type stars in which the SiO $v = 2$, $J = 2-1$ maser was detected (a: NV Aur, b: TX Cam, c: IU Tau, d: V1111 Oph).

the atmosphere to produce SiO masers as noted by S. Ramstedt et al. (2009). The development of circumstellar shells depending on mass loss is another important factor for the detectability of molecular maser and thermal lines in S-type stars. It could be shown that regular pulsations die out and thus mass loss also decreases rapidly at the S-type star stage related to the transition from O- to C-rich stars (F. J. Willems & T. De Jong 1988). As a consequence, O-rich material is no longer replenished in circumstellar shells. These shells continue to expand and dilute, becoming thinner. Nonvariable S-type stars in region IVa may be in this process. We did not detect any maser or thermal lines from any source in region IVa.

The S-type stars are mainly distributed in regions I, II, VII, VIa, and VIb as shown in Figure 3. The distribution of S-type stars in this two-color diagram might be explained by an evolutionary stage of the final O-rich AGB stars in the corresponding loop produced by the four thermal pulses of the M. Steffen et al. (1998) hydrodynamical simulation model. If there is a cycle of change in C/O ratios in this evolutionary loop, a cycle of production of SiO or H_2O masers, including the cycle of O-rich and C-rich chemistry change, may also be formed. However, in the case of the 22 GHz H_2O maser, we did not detect it in any of the 150 sources with our minimum SNR $\sim$ 3, 0.81–1.23 Jy.

5. Summary

1. The observations toward 150 S–type AGB stars (SMASTES II) have been performed with the KVN 21 m single-dish telescopes from 2023 March to 2024 May. Using the upgraded wide four-band (22/43/86/129 GHz) receiving system, we simultaneously observed nineteen molecular lines: H_2O $6_{1,6}$–$5_{2,3}$, ^{28}SiO $v=0,1,2,3, J=$ 1−0; $v=0,1,2, J=$ 2−1; $v=0,1,2, J=$ 3−2; ^{29}SiO $v=0, J=$ 1−0, 2−1; ^{30}SiO $v=0, J=$ 1−0; CS $v=0, J=$ 1−0; HCN $v=0, J=$ 1−0; SiS $v=0, J=5$−4; SO $v=0$, $N_J=2_2$–1_1; and SO_2 $v=0$, $J_{K_a,K_c}=24_{4,20}$–$23_{5,19}$.
2. We detected the SiO $v=1, J=1-0, 2-1,$ and $3-2$ masers from nine, 13, and six sources among 150 S-type stars showing the detection rates 6.0%, 8.7%, and 4.0%, respectively. The SiO $v=1, J=2-1$ maser was detected in more stars than the $v=1, J=$ 1−0 maser, despite requiring a higher rotational excitation energy compared to that of the SiO $v=1, J=1-0$ maser. This trend is the same as in SRs of M-type stars. The detection rates of the SiO $v=0, J=1$–$0, J=2$–$1,$ and $J=$ 3−2 lines increase toward a higher rotational transition from $J=1-0$ to $J=3-2$ like the trend in SRs and Miras of M-type stars.
3. The SiO $v=2, J=$ 2−1 maser was detected from only two S-type stars, V418 Cas (#15) and χ Cyg (#114) although a higher detection rate of H_2O maser is expected due to the absence of line overlap effect between SiO and H_2O. It was the first detection of the SiO $v=2, J=$ 2−1 maser from V418 Cas (#15).
4. HCN line was detected in four S-type stars: S Cas (#16), W Aql (#102), R Cyg (#110), and χ Cyg (#114). SiS, CS, SO, and SO_2 lines were not detected.
5. In particular, no 22 GHz H_2O maser has been detected in any S-type stars among 150 sources despite high detection rates in O-rich M-type AGB stars. This seems to be for the reason that as S-type stars go through the thermal pulse period, the atomic oxygen gradually decreases, which leads to a low OH abundance and a decrease in the formation of H_2O molecules.
6. We investigate the wind velocity profile for 4 HCN detected S-type stars based on simultaneously obtained KVN data. The trend of velocity profile is similar to that for 11 HCN detected O-rich M-type stars. It shows that expansion velocity increases rapidly through the dust layer implying radiation pressure on dust and reaches mass-loss velocities measured by CO expansion velocities. S Cas and W Aql show a rapid acceleration compared to R Cyg and χ Cyg.
7. Fourteen SiO maser and thermal-line detected sources are distributed in O-rich star regions I, II, IIIa, and VII (C-rich star region) near the O-rich star region in the IRAS two-color diagram. Nondetected S-type stars are distributed in regions VIa (mainly C-rich) and VIb (some O-rich). We can try to explain these distributions by adopting an evolutionary sequence of S-type stars from an O-rich M-type stars to a carbon star.

Acknowledgments

This work was supported by a National Research Foundation of Korea (NRF) grant funded by the Korean government (MSIT; S.-H.C.; No. RS-2022-NR069862, D.-H.Y.; NRF2019R1A6A3A01091901, K.-W.S.: 2022R1I1A3055131) and by the Major Project Research Fund (J.K.: No. 2022-1-840-05 and 2023-1-840-02) of the Korea Astronomy and Space Science Institute (KASI). We are grateful to all the staff members at the KVN who helped operate the array and the single-dish telescope and correlate the data. The KVN is a facility operated by KASI, which is under the protection of the National Research Council of Science and Technology (NST). KVN operations are supported by the Korea Research Environment Open Network (KREONET), which is managed and operated by the Korea Institute of Science and Technology Information (KISTI).

ORCID iDs

Seong-Min Son https://orcid.org/0009-0007-1400-7413
Se-Hyung Cho https://orcid.org/0000-0002-2012-5412
Jaeheon Kim https://orcid.org/0000-0001-9825-7864
Hyeon Baek https://orcid.org/0009-0002-9223-8819
Dong-Hwan Yoon https://orcid.org/0000-0001-7120-8851
Kyung-Won Suh https://orcid.org/0000-0001-9104-9763

References

Ake, T. B. 1979, ApJ, 234, 538
Andriantsaralaza, M., Ramstedt, S., Vlemmings, W. H. T., et al. 2021, A&A, 653, A53
Baek, H., et al. 2025, AJ, 170, 84
Bieging, J. H., & Latter, W. B. 1994, ApJ, 422, 765
Boboltz, D. A., & Wittkowski, M. 2005, ApJ, 618, 953
Bujarrabal, V., Alcolea, J., Sánchez Contreras, C., & Colomer, F. 1996, A&A, 314, 883
Chen, P. S., Liu, J. Y., & Shan, H. G. 2019, AJ, 158, 22
Chen, J., Luo, A.-L., Li, Y.-B., et al. 2022, ApJ, 931, 133
Cho, S.-H., & Kim, J. 2012, AJ, 144, 129
Cotton, W. D., et al. 2010, ApJS, 187, 107
Danilovich, T., Ramstedt, S., Gobrecht, D., et al. 2015, A&A, 581, A60
Danilovich, T., Ramstedt, S., Gobrecht, D., et al. 2018, A&A, 617, A132
Danilovich, T., et al. 2021, A&A, 655, A80
Decin, L., et al. 2010, A&A, 516, A69
De Beck, E., & Olofsson, H. 2020, A&A, 642, A20
De Vicente, P., et al. 2016, A&A, 589, A74
Diamond, P. J., et al. 1994, ApJL, 430, L61
Duari, D., Cherchneff, I., & Willacy, K. 1998, A&A, 333, L1
Freytag, B., & Höfner, S. 2008, A&A, 483, 571
Gottlieb, C. A., Decin, L., Richards, A. M. S., et al. 2022b, A&A, 660, A94
Groenewegen, M. A. T., & de Jong, T. 1998, A&A, 337, 797
Gustafsson, B., et al. 2008, A&A, 486, 951
Herwig, F. 2005, ARA&A, 43, 435
Hoai, D. T., et al. 2024, A&A, 692, A86
Höfner, S., Bladh, S., Aringer, B., & Ahuja, R. 2016, A&A, 594, A108
Höfner, S., & Olofsson, H. 2018, A&ARv, 26, 1
Iben, I., & Renzini, A. 1983, ARA&A, 21, 271
Jorissen, A., & Knapp, G. R. 1998, A&AS, 129, 363
Keenan, P. C. 1954, ApJ, 120, 484
Libert, Y., Gérard, E., & Le Bertre, T. 2010, A&A, 515, A112
McDonald, I., & Zijlstra, A. A. 2016, ApJL, 823, L38
Olofsson, H., Rydbeck, O. E. H., Lane, A. P., & Predmore, C. R. 1981, ApJL, 247, L81
Olofsson, H., Rydbeck, O. E. H., & Nyman, L.-Å. 1985, A&A, 150, 169
Plez, B., Van Eck, S., Jorissen, A., et al. 2003, in IAU Symp. 210, Modeling of Stellar Atmospheres, ed. N. E. Piskunov, W. W. Weiss, & D. F. Gray (San Francisco, CA: ASP)
Ramstedt, S., Maercker, M., Olofsson, G., et al. 2011, A&A, 531, A148
Ramstedt, S., Schöier, F. L., & Olofsson, H. 2009, A&A, 499, 515
Ramstedt, S., Vlemmings, W. H. T., Humphreys, E., et al. 2012, in IAU Symp. 287, Cosmic Masers—from OH to H0, ed. R. S. Booth et al. (Cambridge: Cambridge Univ. Press), 260
Ramstedt, S., Mohamed, S., Vlemmings, W. H. T., et al. 2017, A&A, 605, A126
Raskin, G., van Winckel, H., Hensberge, H., et al. 2011, A&A, 526, A69
Rudnitskij, G. M. 1976, SvA, 20, 693
Sahai, R., & Liechti, S. 1995, A&A, 293, 198
Sevenster, M. N. 2002b, AJ, 123, 2788

Schöier, F. L., Ramstedt, S., Olofsson, H., et al. 2013, A&A, 550, A78
Smolders, K., Neyskens, P., Blommaert, J. A. D. L., et al. 2012, A&A, 540, A72
Smith, V. V., & Lambert, D. L. 1990, ApJS, 72, 387
Soria-Ruiz, R., et al. 2004, A&A, 426, 131
Stephenson, C. B. 1984, Publ. Warner & Swasey Obs., 3, 1
Steffen, M., Szczerba, R., & Schoenberner, D. 1998, A&A, 337, 149
Suh, K.-W. 2021, MNRAS, 500, 1117
Ting, Y.-S., et al. 2018, ApJ, 858, 17
Van der Veen, W. E. C. J., & Habing, H. J. 1988, A&A, 194, 125
Van Eck, S., et al. 2000, A&AS, 145, 51
Van Eck, S., et al. 2017, A&A, 601, A10
Vanture, A. D., Wallerstein, G., & Suntzeff, N. B. 2002, ApJ, 569, 984
Wallström, S. H. J., et al. 2024, A&A, 681, A50
Willems, F. J., & De Jong, T. 1988, A&A, 196, 173
Wood, P. R., Bessell, M. S., & Fox, M. W. 1983, ApJ, 272, 99